Irradiation Burst Studies on Belle II PXD Module Components

Jannes Schmitz

Masterarbeit in Physik
angefertigt im Physikalischen Institut

vorgelegt der
Mathematisch-Naturwissenschaftlichen Fakultät
der
Rheinischen Friedrich-Wilhelms-Universität
Bonn

Dezember 2020

I hereby declare that this thesis was formulated by myself and that no sources or tools other than those cited were used.

Bonn, ...
Date Signature

1. Gutachter: Prof. Dr. Jochen Dingfelder
2. Gutachter: Prof. Dr. Klaus Desch

Contents

CHAPTER 1

Introduction

The Standard Model of particle physics (SM) is considered as the most complete theory to describe the observations in our universe[1].

By combining the efforts and discoveries of thousands of physicists, a model was developed over the last century, that contains all known fundamental particles and three out of the four known fundamental forces [1].
It manages to describe almost all experimental observations with remarkable accuracy. Experiments at particle accelerators have played an integral role in testing the SM with even higher energies and precision.

One of these experiments was the Belle experiment, which ran at the KEKB accelerator in Japan between 1999 and 2010 [2].
It was designed to study CP violation in B meson decays. CP symmetry describes the invariance of processes under the combined operation of charge conjugation (C) and inversion of spatial coordinates (parity P). Therefore, a violation of CP symmetry would result in a possible explanation for the observed dominance of matter over anti-matter in our universe.
In 2001, the CP violation was confirmed in the neutral B meson system using the result recorded by the Belle detector [3]. Futhermore, it was validated in the BaBar experiment at Stanford Linear Accelerator Center (SLAC) [4].

This discovery verified the theoretical model of Makoto Kobayashi and Toshihide Maskawa, resulting in the awarding of the Nobel Prize in Physics in 2008 [5].
While the parameters of the Cabibbo-Kobayashi-Maskawa (CKM) quark mixing matrix, that includes CP violation in the SM via flavour changing weak decays, could be precisely measured, thoughts about the completeness of the model emerged [6]. Since observations, e.g. of our primarily matter-dominated universe, were still not compatible with the newest measurements [7], conclusions did hint to new physics beyond the Standard Model. To study even the smallest deviations from the Standard Model and gain highest possible precision while decreasing statistical limitations, accelerator and detector of the Belle experiment have been upgraded between 2010 and 2016 [8].
The innermost layer of the detector was upgraded to a pixel vertex detector (PXD), using the Depleted P-Channel Field Effect Transistor (DEPFET) technology.

During the operation of the detector, several beam loss incidents occurred at the accelerator, leading to matrix irregularities and increased currents of PXD modules. In the scope of this thesis, module components were investigated during reconstructed irradiation burst events. Therefore, three irradiation campaigns have been planned and executed at the Mainz Microtron (MAMI), aiming to identify the damage mechanism and examine possible protection approaches.

Chapter 2 and 3 give an introduction to the composition of the SuperKEKB accelerator and the Belle II detector. In chapter 4, the working principle and layout of the PXD is explained in detail. Therefore, the concept of DEPFET pixels is introduced, together with the readout principle, the required module components and their assembly to final modules. The observations, that have been made at the accelerator in Japan and led to the studies of this thesis, are presented in chapter 5. After the introduction of the measurement setup in chapter 6, the performed irradiation burst studies are finally presented in chapter 7. Chapter 8 provides a final summary about the results and gives an outlook on possible protective measures.

CHAPTER 2

SuperKEKB Collider

SuperKEKB is a circular electron-positron collider located at the High Energy Accelerator Research Organization (KEK) in Tsukuba, Japan.
It is the successor of the KEKB accelerator, which was running from 1999 to 2010 and provided the Belle experiment with electron-positron collisions [2]. In section 2.1, the setup of the upgraded accelerator is introduced. At first, ection 2.2 describes the underlying physical theory and afterwards, details on the upgrade and future plans are discussed in section 2.3.

2.1 Particle Accelerator

Figure 2.1 shows an illustration of the SuperKEKB accelerator.
Electrons are generated by the photoelectric effect and accelerated to an energy of 7 GeV by linear accelerators (linacs). They are injected into the electron storing ring, the so-called High Energy Ring (HER), passing it clockwise.
The positrons are generated as secondary particles, via bremsstrahlung. Therefore, a pre-accelerated electron beam is focused on a 14 mm tungsten target and thus creates high energetic photons by bremsstrahlung [9]. Due to interaction with the target nuclei, electrons and positrons are created in pairs and seperated by a following magnet. The positron beam is accelerated to 4 GeV in the same main linac and injected into the Low Energy Ring (LER) counter clockwise.

Particle bunches of both beams are brought to collisions in the interaction region, where the Belle II detector records events from the provoked electron-positron annihilation.
More information on the detector can be found in chapter 3.

2.2 Beam Energies and Physics

With the upgrade from KEKB to SuperKEKB, the beam energies were adjusted from 8 to 7 GeV for the electron beam in the High Energy Ring (HER) and from 3.5 to 4 GeV for the positron beam in the Low Energy Ring (LER), resulting in a center of mass energy of $E_{CM} = 10.58\,\mathrm{GeV}/c^2$ [10].

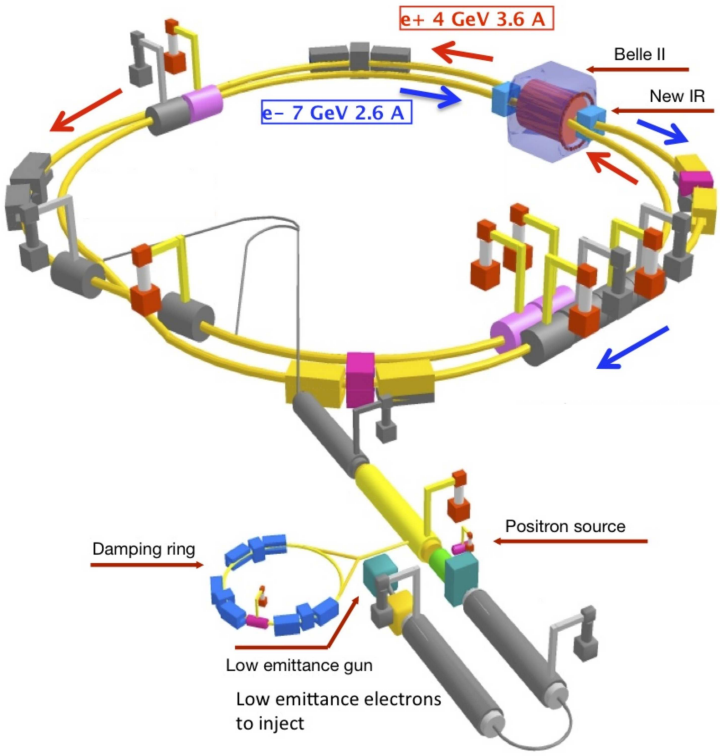

Figure 2.1:
Schematic illustration of the SuperKEKB accelerator [11]. Electrons and positrons are pre-accelerated in a linear accelerator before they are stored in their respective storing ring. e^+ and e^- beams collide within the detector volume at the interaction region.

By fixing the center of mass energy slightly above the $B\bar{B}$ pair production threshold, one can maximize the probability of B meson production. Due to the collision, e^+ and e^- annihilate and produce a quarkonium state of bottom quark and anti-bottom quark, called Υ meson. At the fourth resonance ($\Upsilon(4S)$), which corresponds exactly to the set E_{CM}, the energy is sufficient to produce the excited state of the Υ meson, which then decays into B^+B^- or $B^0\bar{B}^0$ pairs with a branching fraction of $\Gamma_i/\Gamma > 96\,\%$ [12][13]. This leads to clean environment with low background, that is compulsory for this sort of high precision measurements. A possible decay is illustrated in figure 2.2. Since this setup produces primarily B meson pairs, another advantage is the feasibility of accurate reconstruction of the decay kinematics, when one of the two mesons can be detected. Due to the asymmetric settled beam current of LER and HER, the center of mass system is Lorentz boosted with a factor of $\beta\gamma = 0.28$ in electron beam direction. Decreasing this parameter from $\beta\gamma = 0.425$ for KEKB during the accelerator upgrade efforts, the best possible compromise was found between determining the vertices and decay time difference of the two B mesons with highest precision, while having the lowest possible reduction of detector coverage evoked by the distorted solid angle [14][15].

As a result of the relatively low B meson momentum from these decays, all decay products are almost isotropically distributed in the rest frame of the boosted Υ meson [13], which leads to the asymmetric detector design that is covered in chapter 3.

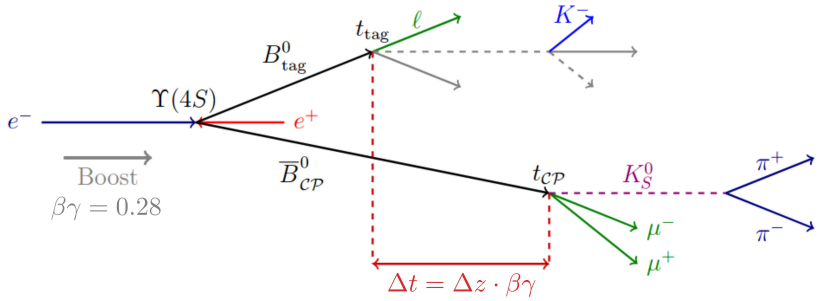

Figure 2.2: Illustration of an event, where two neutral B mesons are produced at the ϒ (4S) resonance. By identifying the decay products, the flavour of the tagging B meson B^0_{tag} can be measured. Reconstructing the secondary vertices and measurements of the decay time difference Δt allows the studies of CP asymmetries. Adapted from [16].

2.3 Luminosity Upgrade

To increase the likelihood of small beyond Standard Model effect observations, the main intention of the accelerator upgrade was the significant increase of luminosity, which translates to higher statistics of the measurement.

The SuperKEKB accelerator is designed for a target instantaneous luminosity of $8.0 \times 10^{35}\,\text{cm}^{-2}\,\text{s}^{-1}$, exploring a new luminosity frontier for collider experiments. To achieve this 40-fold boost of instantaneous luminosity of $2.11 \times 10^{34}\,\text{cm}^{-2}\,\text{s}^{-1}$[17] for KEKB, which already was a world record at this time, two specific machine parameters were selected to tune the accelerator to the target luminosity. Under the assumption of two flat beams with equal horizontal and vertical beam size at the interaction point, the instantaneous luminosity $\mathcal{L}$ of a collider can be described by equation 2.1

$$\mathcal{L} = \frac{\gamma_\pm}{2 e r_e}\left(\frac{I_\pm \xi_{y\pm}}{\beta^*_{y\pm}}\right)\left(\frac{R_L}{R_{\xi_y}}\right). \tag{2.1}$$

Where

- $\pm$ suffix for the positron (+) and electron (-) beam
- $\gamma_\pm$ Lorentz factor
- e elementary charge
- r_e classical electron radius
- R_L, R_{ξ_y} reduction factors, which arise from the crossing angle between the two beams (typical: $\frac{R_L}{R_{\xi_y}} \approx 1$)
- $I_{y\pm}$ total beam current

$\xi_{\pm}$ vertical beam-beam parameter

$\beta^*_{y\pm}$ vertical beta-function

As one can see, the luminosity is mainly determined by the last three parameters $I_{y\pm}$, $\xi_{\pm}$ and $\beta^*_{y\pm}$. These were tuned to the final values shown in table 2.1, based on the new nano beam scheme. In order to maximize the interaction region of two colliding particle bunches, a new final focussing concept was introduced. This so-called QCS system is located close to the interaction point and allows the collision of two extreme narrow beams at a crossing angle of 83 mrad.
More information on the nano beam scheme and determination of machine parameters can be found in [8] and [10].

Parameter	Unit	KEKB		SuperKEKB	
		LER	HER	LER	HER
Energy E	GeV	3.5	8.0	4.0	7.007
Beam Current I	A	1.64	1.19	3.60	2.60
Vertical beam-beam parameter $\xi_{\pm}$	-	0.129	0.090	0.088	0.081
Beam crossing angle	mrad	0 crab-crossing		83 nano-beam	
Vertical beta-function $\beta^*_{y\pm}$	mm	5.9	5.9	0.27	0.30
Luminosity $\mathcal{L}$	$\mathrm{cm}^{-2}\,\mathrm{s}^{-1}$	2.108×10^{34}		8.0×10^{35}	
Integrated luminosity $\int \mathcal{L}$	ab^{-1}	1.041		50	

Table 2.1: Comparison of machine parameters for KEKB and the upgraded SuperKEKB accelerator [8]. The KEKB parameters are the values achieved with the so-called crab-crossing technique, in which crab cavities are used to deflect and tilt the particle bunches close to the interaction point [17]. This results in a head-on collision and an effective crossing angle of 0 mrad. Before commissioning the crab cavities for compensation, the crossing angle of colliding bunches was 22 mrad, limiting the luminosity to $1.76 \times 10^{34}\ \mathrm{cm}^{-2}\,\mathrm{s}^{-1}$ [18].

On the way to reaching target luminosity in 2025, on June 21st 2020, SuperKEKB reached a instantaneous luminosity of $2.4 \times 10^{34}\ \mathrm{cm}^{-2}\,\mathrm{s}^{-1}$, setting a new record for the highest luminosity for a colliding beam accelerator [19].
Further steps in the schedule for peak luminosity and accumulated integrated luminosity can be found in figure 2.3.

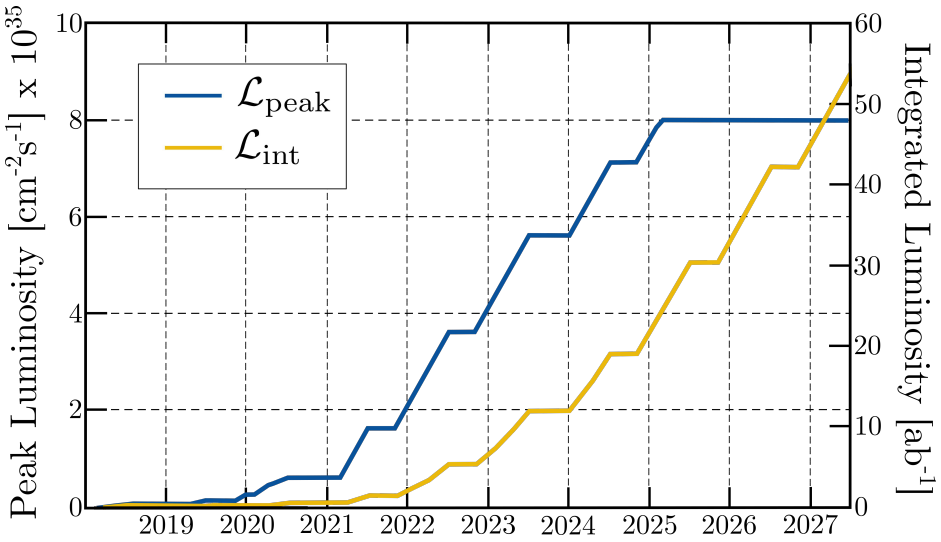

Figure 2.3: SuperKEKB time schedule for increasing luminosity. According to plan, the accelerator will reach the planned peak luminosity of 8.0×10^{35} cm^{-2} s^{-1} in 2025 and accumulate 50 ab^{-1} integrated luminosity until early 2027.

These exceptional numbers can not be achieved without any trade-offs. Not only reduced beam stability could endanger the experiments operation. The luminosity increase is accompanied by a likewise increase of beam-related backgrounds and new requirements for the detector. During the upgrade, the Belle detector was also redesigned to meet the new demands in terms of resolution, occupancy and radiation hardness. The updated detector is introduced in the next chapter.

CHAPTER 3

Belle II Detector

To be able to cope with the new environmental conditions, the structure of the Belle II detector also had to be adjusted. Therefore, new detector technologies were introduced, particularly in the innermost layers. The new design in shown in figure 3.1.

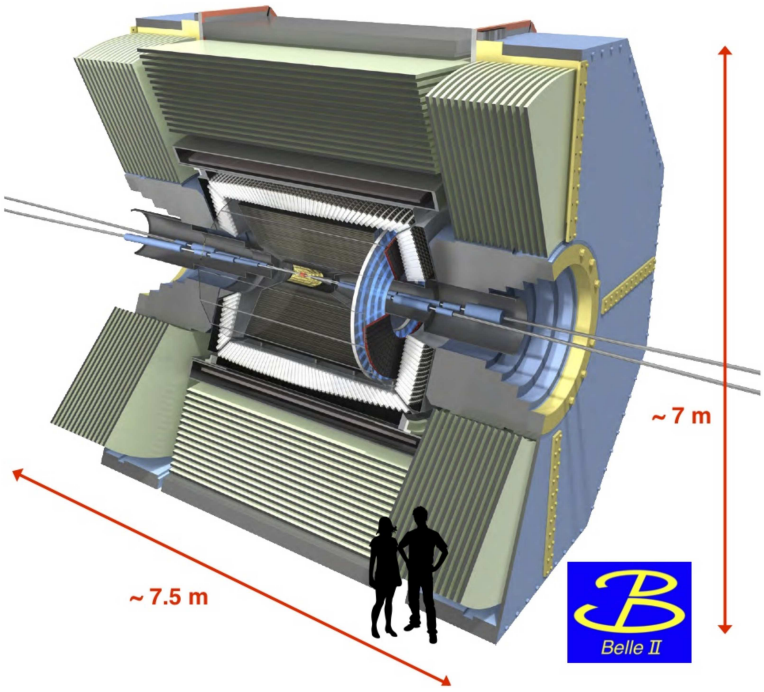

Figure 3.1: Three-dimensional cross section of the Belle II detector [11]. More information on the seven sub-detectors and their positioning can be obtained from figure 3.4.

The upgraded detector, which started data taking in early 2018, consists of seven sub-detectors to cover the measurements of all required physical properties for the decay products, i.e. vertex, track, particle

type and energy. The individual components will be briefly introduced in the next abstract, starting with the outermost part of the detector. If not indicated differently, the information on construction methods and physical fundamentals are taken from the Belle II Technical Design Report [10].
An illustrated overview over the detectors components and their placement can be found in the cross-sectional view in figure 3.4.

K_L and muon counter (KLM)

Furthest out from the interaction point, separated from the inner sub-detectors by the superconducting coils of the 1.5 T solenoid magnet, the KLM detector is capable of identifying muons and long-lived neutral kaons. Using the 4.7 cm thick iron plates of the solenoids flux return yokes as active absorber material, stacked alternating with thin planar resistive plate chambers (RPCs), hadronic showers of the K_L mesons can be induced and detected. Detection of the muons happens via their deposited electromagnetic energy combined with the reconstruction of a charged track in the central drift chamber (CDC,see page 7). In the barrel part, 14 of these iron-plate/active-detector pairs were reused from the Belle-era. Since experience from the predecessor experiment showed that the RPCs could not cope with the strong neutron background rate, endcap and inner two layers of the barrel were replaced with scintillator bars. Each scintillator strip is interspersed with a wavelength shifting fiber and silicon photomultipliers (SiPM) attached thereto, resulting in a high radiation tolerance and the capability of operating in high magnetic fields [20].

Electromagnetic Calorimeter (ECL)

With an inner barrel radius of 1.25 m, roughly 2 m distance in forward and 1 m in backward direction to the interaction point, the electromagnetic calorimeters main purpose is the detection of photons and electrons. In total, 8 736 thallium-doped caesium iodide scintillation crystals with distinct shape and alignment to the IP were recycled together with photodetectors from the predecessor experiment. With an average length of 30 cm, which corresponds to 16.1 radiation lengths X_0, it is essential for high efficiency measurements of photon energies and angular coordinates from neutral hadron decays, e.g. π^0-decays. Hence, the ECL is an integral part of the neutral reconstruction in Belle II, since roughly one third of B meson decay products are neutral hadrons, producing such photons. Beside the identification of electrons and positrons from electromagnetic cascades in the ECL, it is also used for luminosity measurements and trigger generation with the improved high temporal resolution of the upgraded photomultipliers readout. Together with KLM, it is in addition crucial for the detection of the long-lived neutral kaon K_L. In coorperation with the inner tracking detectors, electromagnetic showers induced by charged leptons and photons can additionally be distinguished by mapping tracks to the associated clusters.

Aerogel Ring Imaging Cherenkov Detector (ARICH)

The ARICH detector is one of the two sub-detectors used for particle identification and covers an area of 3.5 m^2 in the forward direction in the endcap region of Belle II [21]. Its operating principle and the proximity-focussing of pion and koan induced Cherenkov cones are shown in 3.2(b). Particle Identification in ARICH is based on the fact, that the Cherenkov radiation angle Θ_C is dependent on the particles velocity, which differs for different particle types at the same momentum. A specially developed silica aerogel is used as non homogenous Cherenkov radiator.

When charged particles traverse through the active medium faster than the phase velocity of light in the medium, they cause the emission of light under the specific Cherenkov angle. By using two aerogel layers with different optical indices as focussing configuration, rings overlap at the readout plane with specific spacing. In 200 mm distance to the crystal, an array of hybrid avalanche photodiodes (HAPD) is used to gain two dimensional information of the Cherenkov intereference rings [22]. This information is not only exploited to discriminate between kaons and pions over most of the momentum spectrum, but also allows for the seperation of the lighter electrons, muons and pions below 1 GeV.

Time of Propagation Detector (TOP)

The Time of Propagation counter (TOP) is a second sub detector, used for particle identification in the barrel region of Belle II. It consists of 16 quartz radiator bars with respectively attached photomultipliers (PMTs) and is especially designed for the reliable distinction between kaons and pions. Each of the light guiding radiators has a length of 260 cm, is 45 cm wide and 2 cm thick [23]. Similar to the ARICH detector, TOP's measurement principle is based on the Cherenkov effect. By using temporal and spacial information of the internally reflected Cherenkov photons, the corresponding particle can be reconstructed and identified. The working principle is shown in figure 3.2(a).

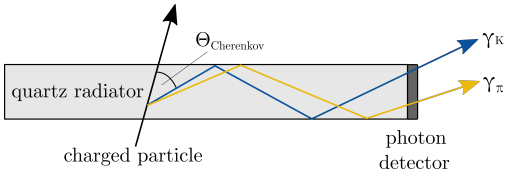

(a) Schematic illustration of the working principle of the TOP detector. Pions and kaons of the same momentum produce photons with different Cherenkov angles, that are internally reflected and then detected by photon detectors. The combined measurement of distance and time of flight allows the discrimination between the two particle types.

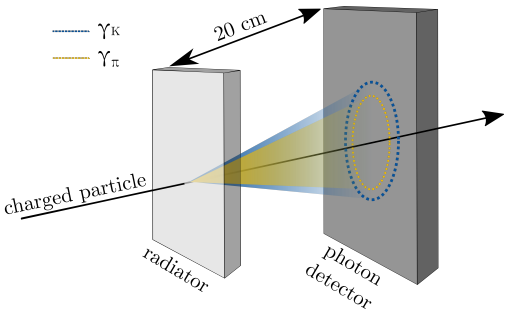

(b) Illustrated working principle of the ARICH detector. Particles trespassing the aerogel radiator generating light cones with velocity dependent opening angle due to the Cherenkov effect. With an array of photomultipliers after 20 cm expansion volume, the Cherenkov angle is measured and used to reconstruct the particle mass.

Figure 3.2: Simplified structure of particle identification sub-detectors TOP (3.2(a)), used in the barrel region and ARICH (3.2(b)), which covers the forward endcap region of the detector in the Belle II experiment. Adapted from [10] and [24].

Central Drift Chamber (CDC)

With its 14 336 sense wires, taut in a cylindrical chamber that covers the detector volume from 16 cm up to 113 cm radius from the IP, CDC is used for track reconstruction of charged particles and the precise measurement of their momentum. In addition to the sense wires, 42 420 field wires with contrary biased voltages traverse the helium-methane (50/50) filled

chamber at different angles [25]. A charged particle passing through will produce electron-ion pairs when colliding with gas atoms. In the vicinity of the sense wires, field wires provide enough energy for the primary electron to ionize further gas atoms, resulting in an avalanche gas amplification. The signal of the electron collecting sense wires is then proportional to the number of primary electrons from ionization of the track and therefore contains the information to calculate the particles energy loss within the chamber. Furthermore, CDC provides trigger signals for charged particles and information to identify low-momentum particles, that do not reach the outer detectors for particle identification. The construction method of the central drift chamber is very cost efficient, but yet provides high spacial resolution over a large volume. Therefore, only small adjustments, e.g. a denser wire configuration, have been made during the upgrade from Belle to Belle II.

Silicon Vertex Detector (SVD)

The Silicon Vertex Detector is another sub-detector, which was redesigned during the detector upgrade in order to withstand the new circumstances in terms of occupancy and readout speed. It consists of four layers double-sided silicon strip sensors, that are arranged cylindrically around the beam pipe at radii of 38, 80, 115 and 140 mm [26]. As depicted in figure 3.4, the outer three layers are angled in forward direction, in order to cover the full polar angle from 17° to 150°. The operating principle of a single sensor, that consists of a silicon bulk with perpendicularly attached p- and n-doped semiconductor strips, is shown in figure 3.3(a). Ionizing particles traversing the silicon bulk will create electron hole pairs along their path, drifting to p-side and n-side respectively. By reading out the strip signal, precise spatial information of the particle track can be obtained in two dimensions. In avoidance of the spread of electrons and holes induced by the Lorentz force of the solenoids 1.5 T magnetic field, sensor planes are slightly tilted. That way also angular occupancy can be maximized, resulting in a windmill like structure enclosing the beam pipe (see figure 3.3(b)).

Pixel Vertex Detector (PXD)

Together with the SVD, the PXD forms the new Vertex Detector (VXD) with the purpose of reconstructing decay vertices and contributing to the tracking. With two layers of sensors at 14 mm and 22 mm radius, the Pixel Vertex Detector is the innermost sub-detector of Belle II. Since the adjustments of beam energies during the luminosity upgrade reduced the Lorentz boost by a factor of 2/3 [10], the evoked narrowed separation between B meson vertices demanded the upgrade to pixel sensor technology for the inner layers of the VXD.

As this thesis deals with investigation of irradiation impacts on PXD modules, the next chapter will introduce structure and operation of the sub-detector more precisely.

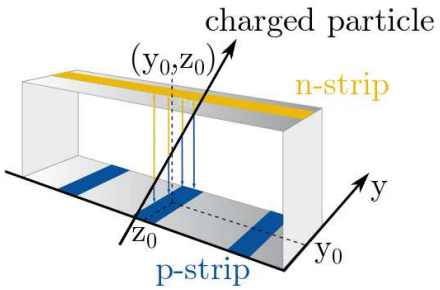

(a) Basic principle of operation of a silicon strip detector. Ionizing particles crossing the silicon bulk will generate charge carriers along their path. Charge collection information of the perpendicular n- and p-doped semiconductor strips then allows for particle localization. Adapted from [16].

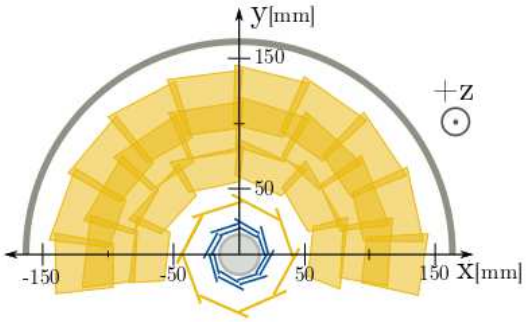

(b) Illustration of the cylindrical arrangement of PXD and SVD layers surrounding the beam pipe at radii between 1.4 cm and 13.4 cm. The two PXD layers are coloured blue, yellow areas depict modules of the four SVD layers. In order to maximize the angular occupancy, ladders are grouped in a windmill like structure around the IP.

Figure 3.3: Working principle and arrangement of the double-sided silicon strip sensors.

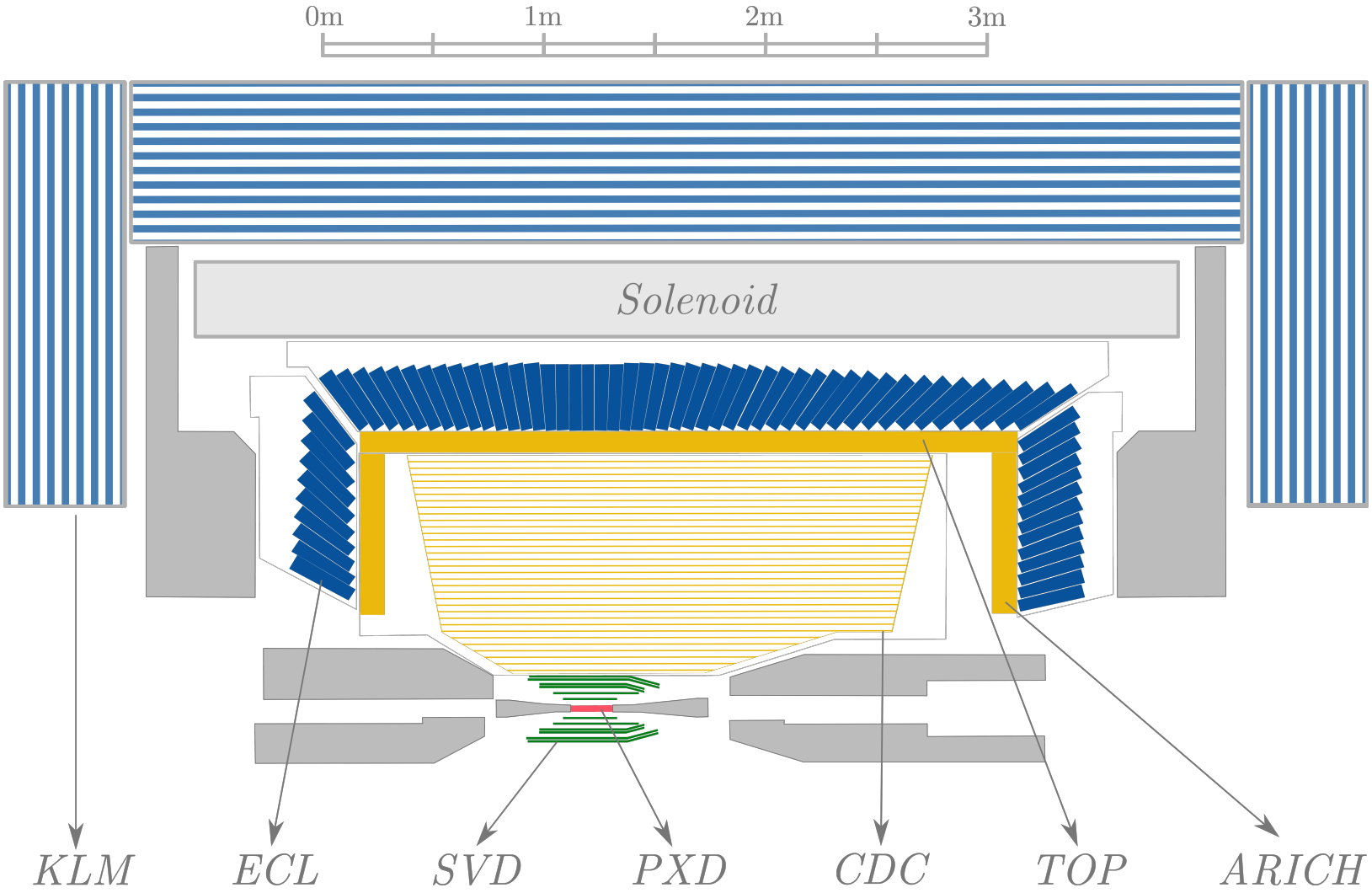

Figure 3.4: Schematic cross-sectional view of the upper half of Belle II and the positioning of its sub-detectors. Adapted from [10, p. 14].

CHAPTER 4

Pixel Vertex Detector (PXD)

With the planned increase of luminosity and associated significant increase of beam backgrounds, efforts on the design of the new detector's interaction region (IR) were quite challenging. Although the beam pipe radius at IP could be halved to 10 mm, the available space for services is severely reduced due to the new final focussing quadrupoles (QCS) [10].

Calculations from the adjustment of accelerators machine parameters yield an estimate of a twentyfold increase for beam-induced backgrounds [27]. Accordingly, an upgrade of the innermost vertex detector was inevitable.

The challenging requirements for the new technology were [10]:

- high position resolution for vertex reconstruction
- fast readout and efficient operation in the increased background environment
- high radiation hardness
- maintaining mechanical stability while keeping the material budget low to minimize multiple scattering
- coverage of the full angular acceptance $17° < \Theta < 150°$

Even though the main concept of vertex detectors, composed of pixel and strip technology, was already established in other particle physics experiments, SuperKEKB's comparable low energies dictated an even thinner, new sensor design.
With a thickness of only 75 µm [10] and very little power consumption, that makes cooling in the active volume dispensable, the choice fell on monolithic active DEPFET structures [28].
The following chapter will introduce the DEPFET technology used in PXD.
After the general description of the working principle of a single DEPFET pixel cell (4.1.1) and its readout mechanism (4.1.2), the different readout ASICs and their application will be discussed in section 4.2.
Finally, construction and assembly of entire modules, in particular with attention to distinctions between final PXD9 (4.3.2) and scaled-down lab-test modules (4.3.1) is reviewed in section 4.3.

4.1 Depleted P-Channel Field-Effect Transistor (DEPFET)

The concept of depleted field-effect transistors (DEPFETs) as semiconducting detection and amplification devices was first published by Josef Kemmer and Gerhard Lutz in 1987 [29].

4.1.1 Working Principle of a DEPFET Pixel

A DEPFET pixel consists of an n-doped silicon bulk, that acts as detector substrate in case of full depletion. Therefore, sufficient negative voltage has to be applied at the p^+ implant at the backside. On top of the detector substrate, a p-channel Metal-Oxide-Semiconductor Field-Effect Tranistor (MOSFET) is integrated. A potential minimum is formed 1 µm below the external FETs gate [10] with an additional n implant. It is considered as additional internal gate of the transistor. A three-dimensional cross-section of a pixel cell is depicted in figure 4.1.1.

An ionizing particle traversing the pixel cell will generate electron-hole pairs along its path. The depletion voltage of the silicon bulk causes the holes to drift to the p^+ backside. Electrons are attracted and collected by the internal gate. The collected charge alters the potential of the internal gate and eventually modulates the DEPFET source-drain current I_{DS} by inducing image charges [30]. This leads to a non-destructive readout of the signal, that increases linearly with the particle's amount of ionization.
The internal amplification g_q describes the current response to a single electron collected in the internal gate and can be derived by [31]:

$$g_q = \frac{\partial I_{DS}}{\partial q} = \sqrt{\mu_h \frac{I_{DS}}{L^3 W C'_{oxide}}} \tag{4.1}$$

with μ_h : charge carrier mobility

L, W : length and width of the gate

C'_{oxide} : oxides sheet capacitance

I_{DS} : source-drain current

With prototype sensors, g_q values of 400 $\frac{pA}{e}$ [32] up to 560 $\frac{pA}{e}$ [33] have been achieved during test beam campaigns. Each signal electron in the internal gate increases the drain current by roughly 500 pA, which makes further external amplification at the first stage redundant.
This internal amplification is, together with the excellent noise performance provided by the small capacitance of the internal gate, the essential feature of the DEPFET technology.
A punch-through contact, in form of a neighbouring n^+ implant, allows the reset of a pixel after charge collection. Clear pulses with an amplitude of 15 V relative to source voltage are sufficient to cause conductivity between internal gate and the clear implant [16]. Signal electrons will drift to the clear contact and the internal gate is cleared to prepare the pixel for the next measurement.

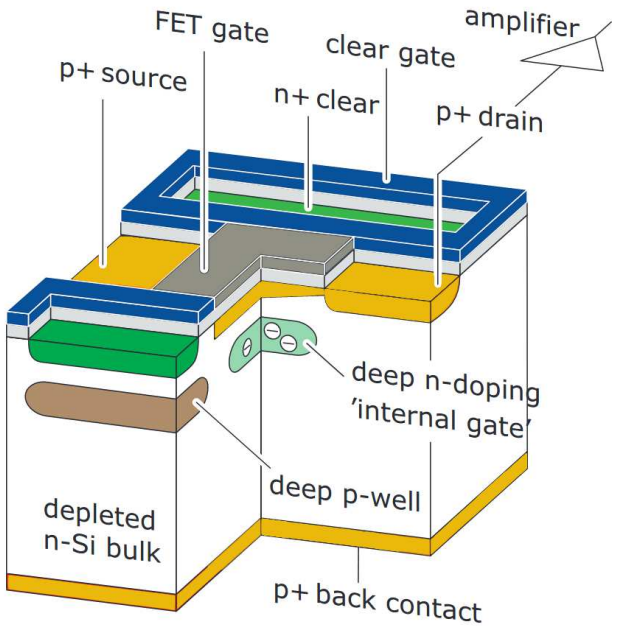

Figure 4.1:
Schematic three-dimensional cross-section of a DEFPET pixel cell. The sensor is based on MOSFET structure, integrated in a sidewards depleted silicon bulk. It combines detection and amplification of signal electrons. These are generated together with holes by traversing ionizing particles and drift towards the internal gate created by an additional n implant. Electrons in the internal gate finally modulate the transistors source-drain current and can be cleared via a positive voltage on the clear implant. Adapted from [34].

4.1.2 Readout Mechanism

To read out large arrays of DEPFET pixels in a short time, the following design was devised for the PXD.
Figure 4.2 shows a 2x2 pixel cell. Each of the four pixels is indicated by seperating yellow dotted lines. Two pixels share a common source implant, forming a double cell. Each clear implant is connected to 4 DEPFET pixels, resulting in the so-called PXD9 design. The positioning of the clear implants, enclosing each internal gate from both sides, allows a faster and more efficient clear process [35].
To read out the pixel matrix, the DEPFET pixels are activated row-wise, while the modulated drain current is read out column-wise. Figure 4.3(a) describes the readout process, which is controlled by the gate and clear voltages.
The matrix is read out in a rolling shutter fashion. To manage a full frame readout in 20 µs multiple pixel rows are read out at the same time. In a four-fold readout scheme, four consecutive matrix rows are connected to a single clear and gate control-voltage each, reducing the readout time by a factor of four [10]. However, the number of drain lines has to be increased by a factor of four. Figure 4.3(a) shows a simplified sketch of the four-fold rolling shutter readout.
Four DEPFET pixel rows are enabled by applying a negative voltage (relative to source) to gate output n, shown in blue. Indicated by red arrows, drain currents of the active pixels are then read out for further processing. After sampling, the clear pulse is applied at clear output n (yellow), removing the charge from the internal gates of the active rows. The readout of the first four matrix rows is completed by setting back the external voltage at gate output n, switching off the respective transistors. By repeating this procedure with all following quadruple-rows, the whole pixel matrix of a PXD module is read out consecutively within 20 µs [10].
Since only four rows of pixels are active at any given time, the power consumption of the matrix is kept low (0.4 W for 800 columns) [10].

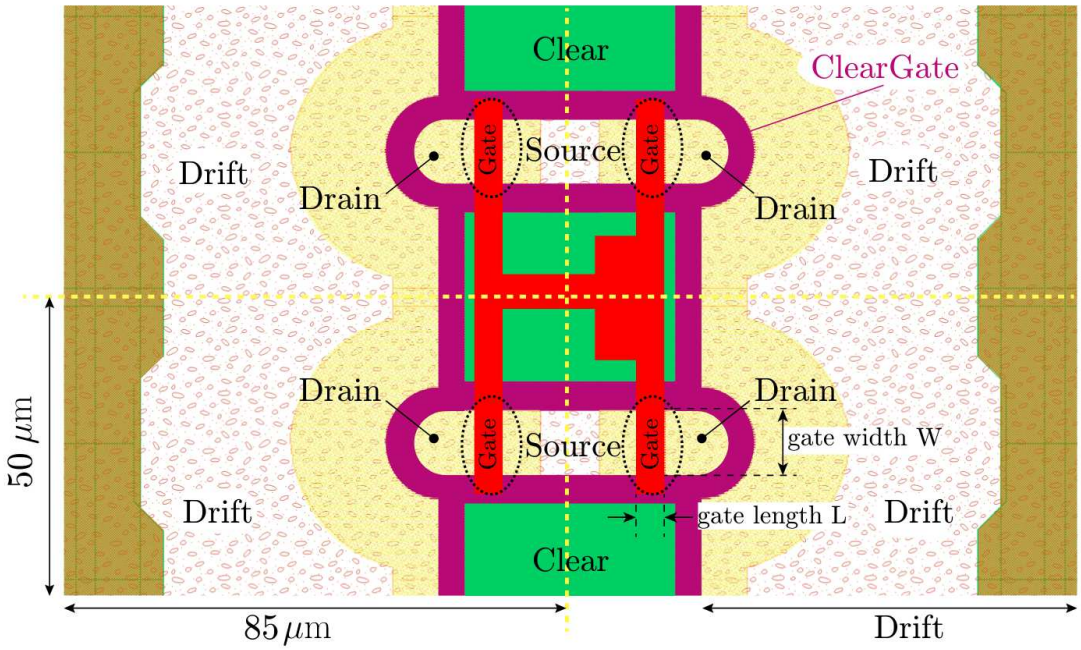

Figure 4.2: Illustration of the four-fold DEPFET pixel design, used for PXD. Yellow dashed lines indicate the segregation between the individual four pixels. The geometrical arrangement allows a space-saving design, since source implant and clear implant can be shared among multiple single pixels [16, p. 85]

The sampling process explained in the last few paragraphs is called single sampling readout. It is illustrated in figure 4.3(b).
To obtain the real signal current from the output of the drain lines, it is compulsory to know the dark current of the active pixel with no electrons in the internal gate. This value is called pedestal current I_{ped} [16].
The natural approach would be a double sampling readout. With an additional second readout shortly after the clear process, the pedestal current is known for each pixel and could be subtracted from the offset affected first sample [32]:

$$I_{\text{signal}} = I_{\text{signal+ped}} - I_{\text{ped}} \tag{4.2}$$

As timing limitations rule out the double sampling method, the solution is found in a compromise, where pedestal values are first measured and cached. Subsequently measured signals can then be calculated by subtracting these average pedestal currents [16].

$$I_{\text{signal}} = I_{\text{signal+ped}} - \left\langle I_{\text{ped}} \right\rangle \tag{4.3}$$

As a disadvantage of the faster readout, this requires frequent upload of new pedestal values. Temperature irregularities or radiation can lead to changes in the sensitivity of the transistor and its currents. Signal quality is now directly linked to the quality of cached pedestal values [36].

The electronics needed to control and read out the modules in above mentioned manner, will be discussed in the next section 4.2.

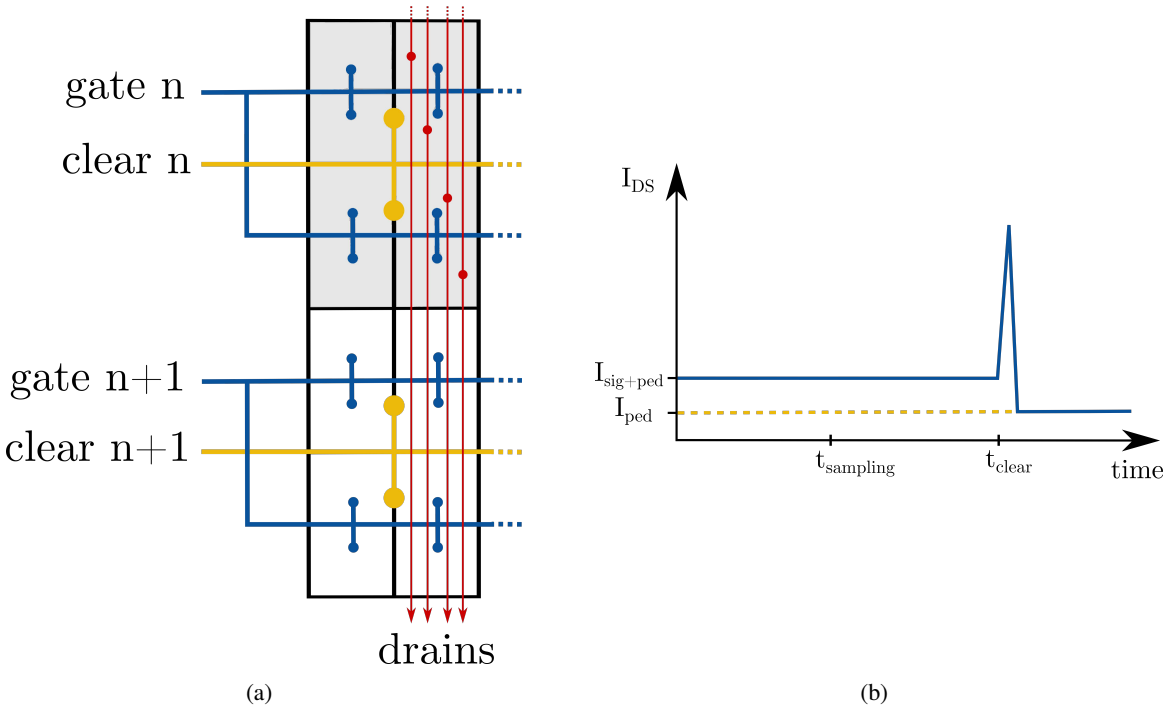

(a) (b)

Figure 4.3: (a) Schematic illustration of the four-fold rolling shutter readout. (b) Behavior of the DEPFET drain current during the single sampling readout. Before a measurement starts, pedestal values have to be cached in order to reconstruct the real signal current. Adapted from [16].

4.2 Application-Specific Integrated Circuits (ASICs)

In addition to the sensor, multiple application-specific integrated circuits (ASICs) are needed to process and control the matrix signals described in section 4.1.2. The overall picture of ASIC communication and composition for modules of the Belle II PXD will be covered in section 4.3.2.
This section will introduce the various ASICs and their functionality in more detail.

4.2.1 Switcher

As depicted in figure 4.3(a), DEPFET matrix control is enabled via gate and clear lines. Therefore, a chip is needed, that is able to independently steer two outputs per quadruple row, with high and low voltage level each. These channels will then be enabled consecutively in order to control the readout of the pixel matrix.
For the Belle II PXD, the *Switcher-B18v2.1* ASIC was designed to fulfill all requirements [37]. Each Switcher has 32 output channels for clear and gate, respectively. Supply of the large voltage range, necessary for the DEPFET pixel (see table 4.1), has to be accomplished. Fast timing and radiation hardness requirements complicate the design.

A photograph of the chip's bottom side is shown in figure 4.4.

output signal	voltage level
ClearOn / `ClearHIGH`	19 V
ClearOff / `ClearLOW`	5 V
GateOn / `GateLOW`	–3 V
GateOff / `GateHIGH`	5 V

Table 4.1: Standard voltages for PXD9 DEPFET operation. All voltages are referenced to source potential.

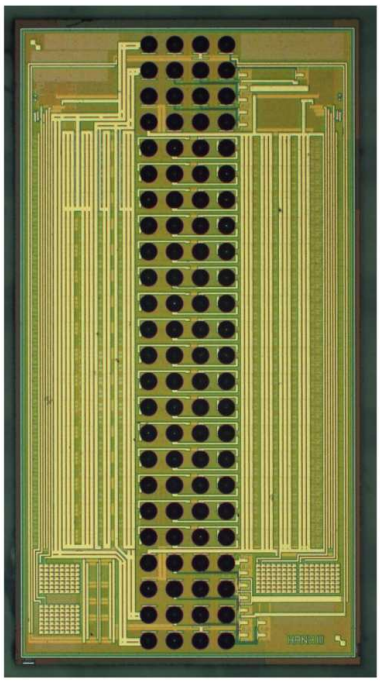

Figure 4.4: Photograph of the Switcher ASIC footprint. The upper and lower areas of 4x4 bump pads connect to the IO signals, while the central 16x4 bump pads are the Switcher outputs. The exact allocation of specific pads can be obtained from [37].

The dimensions of the ASIC are 1 530 µm x 3 360 µm [37]. It is equipped with a 4x24 grid of bump pads to connect to power, control and output lines.
The Switcher is steered by four differential control signals [16].

`SerIn`
The `SerIn` signal provides the frame synchronization. The Signal is propagated through a 32 bit shift register by the clock. The presence of the `SerIn` signal prompts the corresponding Switcher output channel to be activated.

`Clock`
The clock signal synchronizes the operation to the other circuits. One clock cycle corresponds to the readout of one quadruple-row and takes 105 ns [16].

StrG
The StrG signal is one of the two fast strobe signals, that activate the high voltage switches for the chosen channels [37]. When triggered, while Clock is low, the GateLOW / GateOn signal is applied to the associated output channel. At the next rising edge of the StrG signal the current quadruple row is deactivated by applying the GateHIGH / Gateoff signal and the next Switcher channel is activated [16].

StrC
The StrC signal is the corresponding fast strobe signal, that activates the HV switches of the clear channels. When triggered while Clock logic level is high and gate voltage already at low potential (GateLOW / GateOn), ClearHIGH voltage (ClearOn) is applied at the associated output channel [16].

To ensure the control of pixel matrices with more than 128 quadruple rows, multiple Switchers can be daisy-chained [36]. With the SerOut signal, the switching ASICs can be used in series, by forwarding the serial input signal to the next Switcher. For a DEPFET matrix with $4n$ matrix rows, the stored sequence will be executed for each of the n quadruple rows. (The sequence is the same for all n channels, with the exception of the SerIn signal, that is only applied once per cycle) [16].
A schematic illustration of the control signals, together with the resulting output signals, that trigger PXDs rolling shutter matrix readout is shown in figure 4.5.

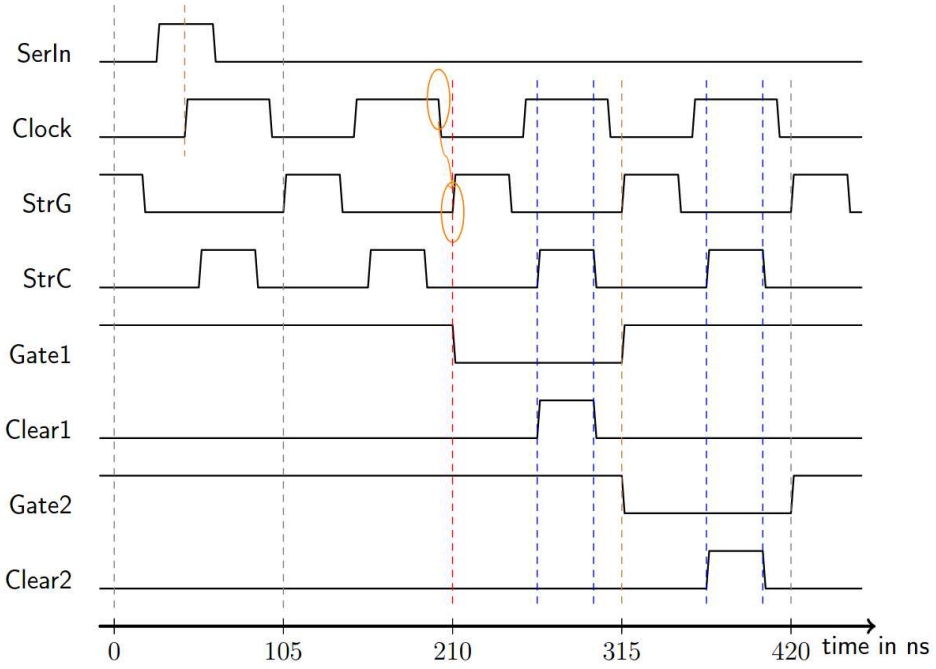

Figure 4.5: Schematic diagram of wave forms and resulting outputs of the PXD9 Switcher sequence. Specifications, that have to be fulfilled by the Switcher sequence, are highlighted. The StrG signal can only be applied, when Clock level is low (orange circles). StrC must be applied, while Clock level is high and the gate is enabled. This results in switching of the activated Clear channel to its high voltage level (ClearOn / ClearHIGH). The first output channel is activated two clock cycles after the SerIn signal [16].

4.2.2 Drain Current Digitizer (DCD)

As the name already indicates, the DCD's task is the digitization of the DEPFET's modulated source-drain currents.
The chip takes up an area of 3.2 mm x 3.2 mm and provides 256 analog inputs. After digital processing and multiplexing to the parallel outputs of the DCD, 8-bit precision at a sampling rate of 105 ns can be achieved by the internal pipeline analog digital converters (ADCs) [38].

Due to the restricted ADC input range of 20 µA up to 40 µA, the DCD provides the option of offset correction before digitalization. As stated in section 4.1.2, the measured drain current is a composition of the real signal from electrons in the internal gate (I_{signal}) and the offset transistor current (I_{ped}). Since I_{signal} only accounts for approximately 10 % - 15 % of the measured drain current ($I_{signal+ped}$), subtraction of adjustable offset currents is obligatory [16].

4.2.3 Data Handling Processor (DHP)

The Data Handling Processor (DHP) processes the digitized data and controls the DCD and Switcher ASICs.
Main features of signal procession and data reduction are pedestal subtraction, zero-suppression and common mode correction. The previously described pedestal subtraction is performed within the DHP. Therefore, specific memory space is allocated for the pedestal data, that need to be cached beforehand. The signal is extracted by subtracting the pedestal values from the values in the raw data memory [39].

Zero-suppression is another method used for data reduction. It restricts the amount of processed information on pixels, that still show signal current after pedestal subtraction. Pixel data without charge signal will be discarded to achieve the dictated data reduction from 20 Gbps input to 2 Gbps output rate [39]. This limitation is mainly caused by the experiment's amount of cables and their length.

Common mode (CM) noise describes noise, that affects every pixel within one quadruple row. In order to filter for this noise, the so called "two parse average" method is used. In a first step, the average over the whole data set is calculated and values that exceed the estimation are replaced with this first common mode value. Within the second step, the average is calculated again ("unbiased CM") and subtracted from the signal values. As a last step, every value is compared to a threshold value. Only the information of pixel data above this threshold will be further processed off module. The corrected and reduced data is stored in a buffer together with a frame header that contains information on the data type and is provided by the DHP [39].

When receiving a trigger signal, the data is sent to the data acquisition system (DAQ) via Low Voltage Differential Signaling (LVDS) lines. Moreover, the DHP itself and its registers are configurable via LVDS lines, using the Joint Test Action Group (JTAG) protocol.
The ASIC communication scheme is completed by the controlling functions of the DHP. It steers the matrix readout by generating synchronizing clock signals for DCD and Switcher ASICs in addition to providing the switcher sequence [39].

The next chapter will discuss the module layout of scaled-down lab-test modules called Hybrid5 and the final PXD9 modules, that are mounted in the Belle II pixel detector.
Illustrations of ASIC positioning and communication scheme for the two module types can be found in pictures 4.6(b) and 4.8.

4.3 Module Layout

This section covers the layout of modules that are assembled with a DEPFET matrix and the introduced control and readout electronics.
For reasons of simplicity, the layout is first discussed for the scaled-down modules, called Hybrid5. In section 4.3.2, the demonstration is then scaled up to describe the modules that are used for the Belle II PXD.

4.3.1 Hybrid5 Modules

The Hybrid5 system is a demonstrator system used for laboratory tests. It consists of a downsized DEPFET matrix and one ASIC of each type. Therefore, it offers an excellent opportunity to study the system's behavior.
A picture of the printed-circuit-board (PCB), on which the components are mounted, together with a simplified illustration of the communication sequence is shown in figure 4.6(a).

Data lines are outlined in yellow, while blue lines indicate command lines.
The mini-matrices consist of 64x32 DEPFET pixel cells and share most of their properties with the large, final PXD matrices. Four different pixel pitches are available: (55 µm x 50 µm), (60 µm x 50 µm), (70 µm x 50 µm) and (85 µm x 50 µm) [16].

A single Switcher ASIC can provide gate and clear voltages to the 16 matrix quadruple rows. The DCD then digitizes the signal currents of the 128 drain lines. Both, Switcher and DCD, are configured and controlled by a single DHP, as illustrated in figure 4.6(b).

Figure 4.6(b) also includes the off-module components, that complete the laboratory measurement setup. The Data Handling Engine (DHE) is the missing piece, that connects the system to the computer's software interface. It generates the DHP system clock and controls the data taking with synchronization and trigger commands.
A custom made power supply (LMU PS) provides the Hybrid5 system with all 23 required voltages and can also be interfaced via Ethernet connection.

Two additional breakout boards are necessary in the laboratory setup to convert between different cable types. They are omitted for the sake of simplicity.

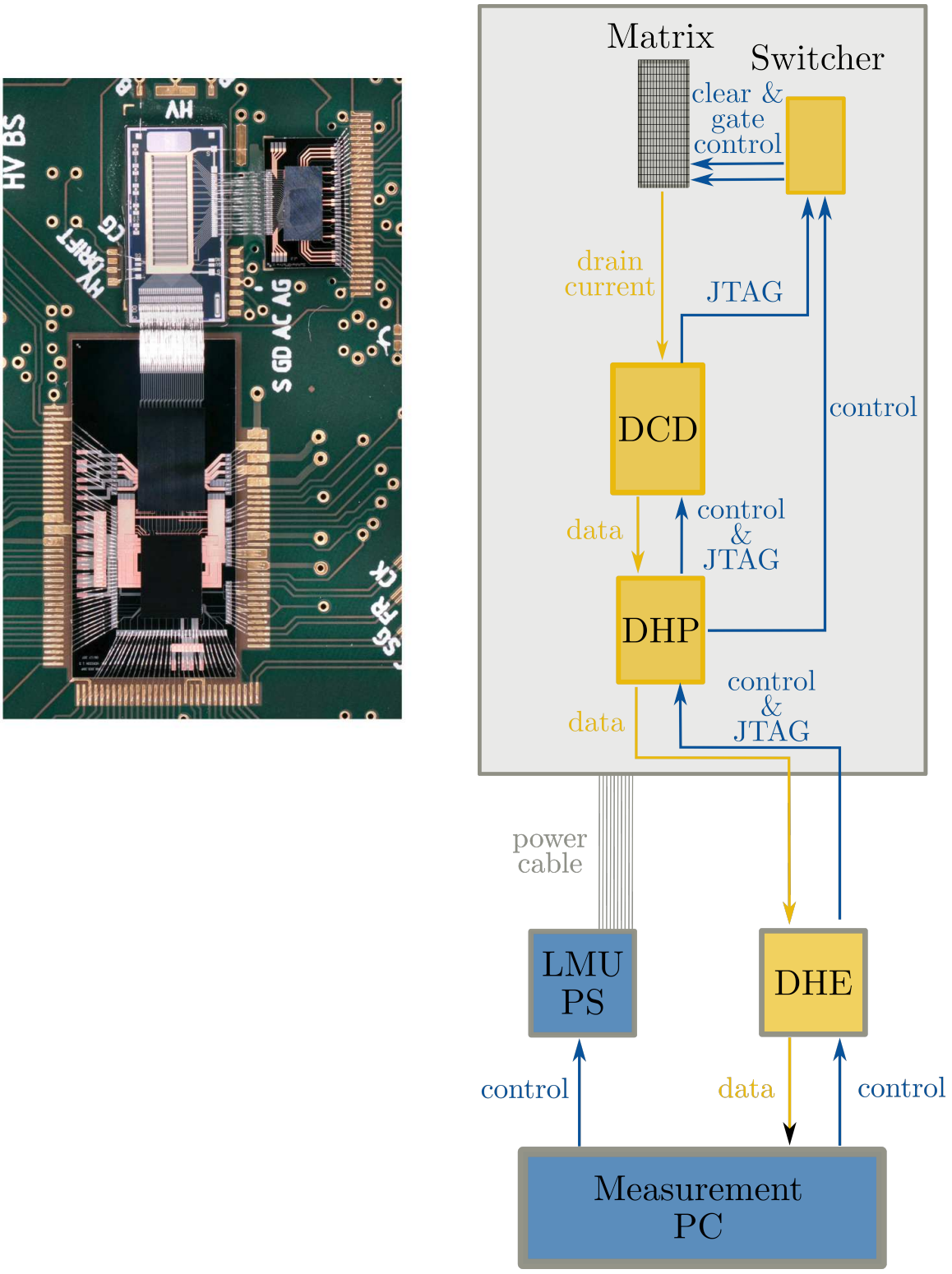

(a) (b)

Figure 4.6: (a) Zoomed in photography of a Hybrid5 module. (b) Full readout scheme of the Hybrid5 system. The gray box in the upper area represents the picture excerpt from (a).

4.3.2 PXD9 Modules

The PXD9 modules are customized for the operation in the Belle II detector.

The supporting wafer structure is made from silicon. As shown in figure 4.7, the material at the sensitive area is thinned down to 75 µm, while the support structure is kept with a thickness of 525 µm. It also includes the position of the Switcher ASIC.

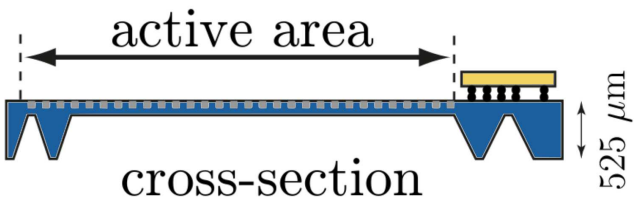

Figure 4.7: Cross section of a PXD9 module. The active area is thinned down to 75 µm. The support structure carries the Switchers and is kept at a thickness of 525 µm [16].

As also visible in figure 4.8, DCDs and DHPs are located at one end of the module outside the tracking region to minimize the material budget close to the IP. This so-called "end of stave" is the mounting point for each module in the final detector (see figure 4.9). The Switchers are located at the long edge of the module, called balcony. In total, six Switcher ASICs are daisy-chained to control the DEPFET matrix with 250 columns and 768 rows. The drain currents of the resulting 1 000 drain lines are digitized by 4 DCDs and pre-processed by 4 DHPs, as described earlier.

Unlike the mini-matrix of the Hybrid5 system, the PXD9 matrix does not only feature DEPFET pixel cells with one specific pixel size, but is seperated in two areas with smaller and larger pixels. The idea is to have smaller pixel pitches closer to the interaction point.

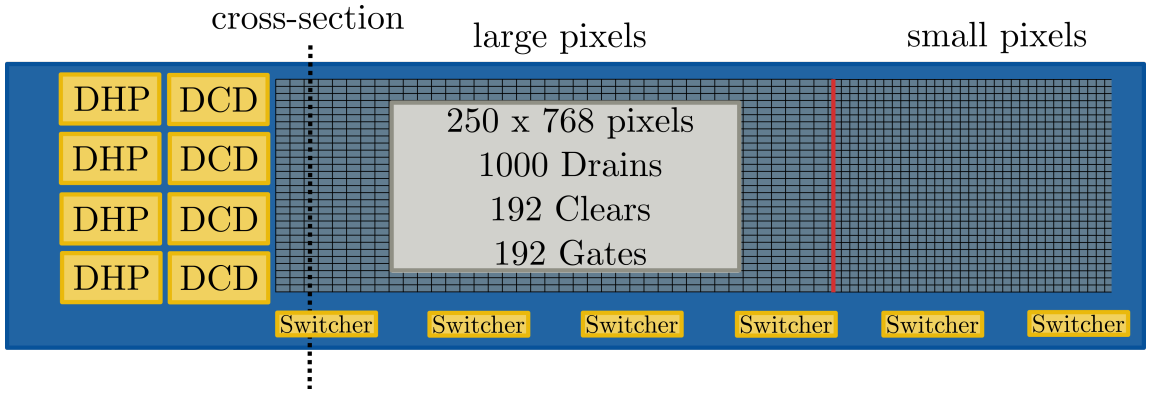

Figure 4.8: Illustration of a PXD9 module layout. The red line represents the boarder between smaller and larger pixel sizes. The cross section showed in figure 4.7 is taken at the dashed line through the first Switcher from the left-hand side. Adapted from [16].

PXD consists of two layers. Each layer consists of ladders arranged in a windmill structure around the beam pipe. A ladder consists of two modules glued end-to-end. There are four different module designs to build the pixel detector.

These four designs are called inner forward (IF), inner backward (IB) for the inner layer and outer forward (OF) and outer backward (OB) for the outer layer of PXD. The main difference is the ASIC layout and therefore metal routing, in order to have a symmetrical ladder design for forward and backward modules.
Since the outer ladders have to be longer to cover the same angle, they feature larger pixel pitches.

Figure 4.9 shows a CAD model of the planned composition of 8 inner ladders and 12 outer ladders, forming the Belle II pixel detector.

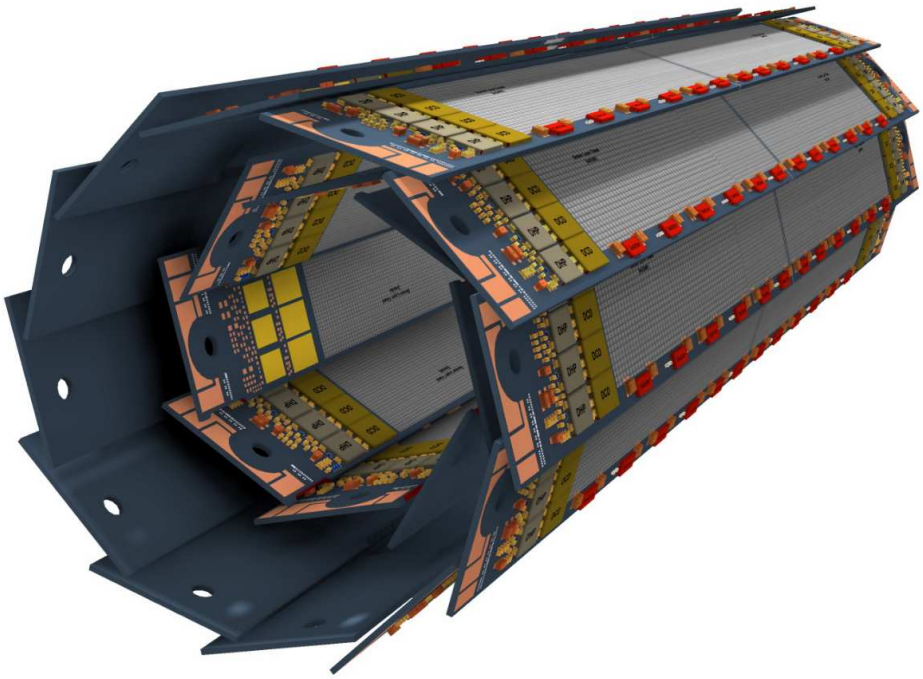

Figure 4.9: CAD model of the PXD design. The inner layer consists of 8 module ladders, enveloped by 12 outer ladders forming the outer layer [16].

Due to a high failure rate in ladder gluing and a shortage in outer modules, the outer part of PXD is reduced to two left ladders at the present time.
In such big projects, problems can not only occur during production, but also during nominal operation, which forms the topic of this thesis.

These problems are outlined in the next chapter.

CHAPTER 5

Measurement Motivation

This chapter introduces the problems, that occurred during detector operation at KEK and the studies performed over the course of this thesis.
It is divided into two sub-sections.
Section 5.1 describes an observation of inefficiencies in the matrix response after beam loss events.
Section 5.2 deals with additional current in the high voltage (HV) channel that occurs with progressing irradiation.

5.1 Matrix Damage after Beam Loss Events

Several major beam losses in the SuperKEKB accelerator led to quenches in the final focusing magnets and permanent damage in PXD over the last one and a half years.
The loss of beam current within 40 µs led to an effective dose of approximately 500 rad for the PXD modules. Resulting in inefficient matrix quadruple rows, PXD suffered an overall loss in efficiency of ~ 3 %, due to such events.

Besides an increase in Switcher currents for the affected modules, the recovery of previously damaged quadruple rows has been observed. The damages only occur in groups of four rows. Therefore, damaged Switcher channels or effects on matrix gate and clear lines are possible sources of error.
Figure 5.1 shows the matrix response of the inner 15 PXD modules after the beam incident in May 2020. Newly occurred inefficient matrix rows are highlighted in blue, while yellow frames indicate recovered quadruple rows.

Investigations after the latest beam incident with serious consequences showed that the occurring inefficiencies are not distributed equally over all matrix rows. A histogram of damaged Switcher channels is shown in 5.2. Switcher channel at the `SerOut` side of the Switcher seem to be more sensitive to the prompt irradiation burst during beam losses.

During this thesis, three irradiation campaigns at the Mainz Microtron were planned and carried out to investigate the damage mechanism and test potential protective measures.

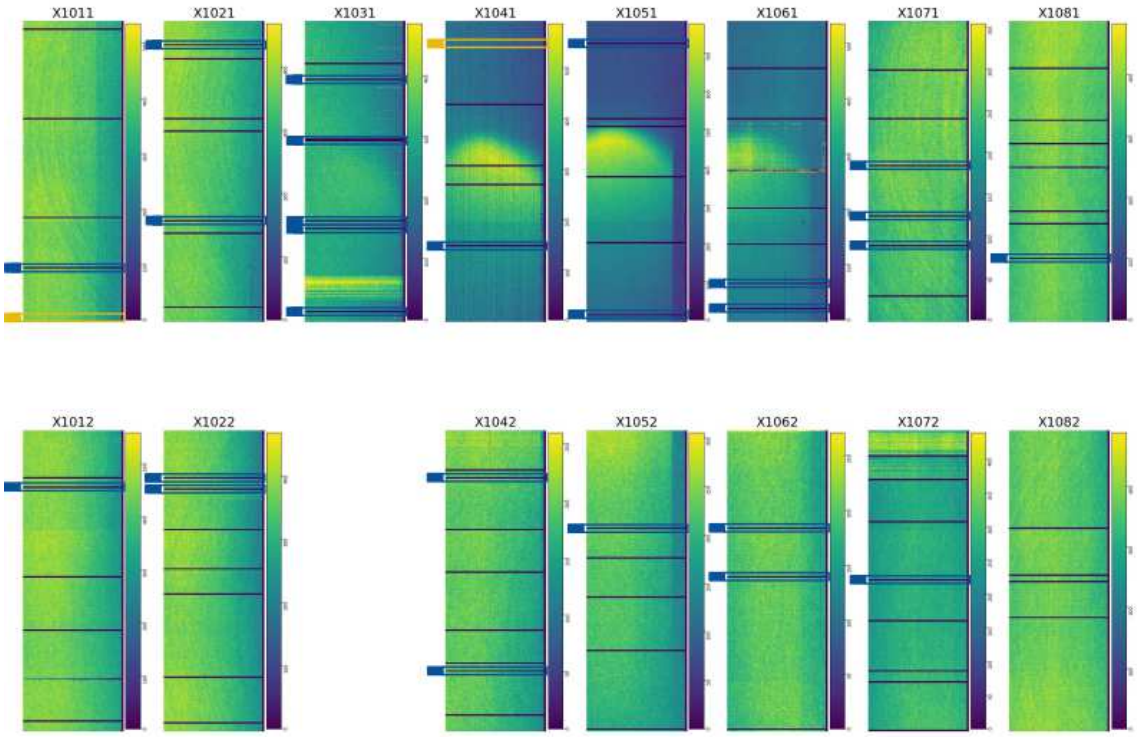

Figure 5.1: Damage pattern of PXD modules after beam incident on 27th of May 2020. Due to beam loss and resulting QCS quench, the pixel vertex detector suffered severe damages. Freshly emerged inefficient quadruple rows are highlighted in blue, while yellow flags indicate recovered rows.

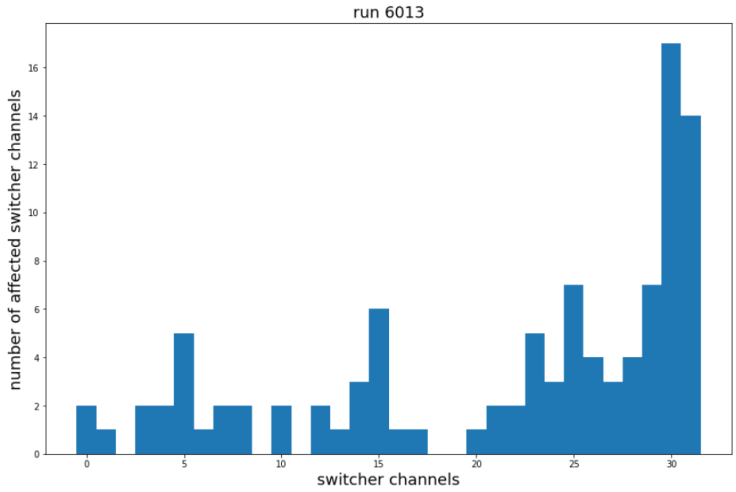

Figure 5.2: Distribution of damaged Switcher channels taken from KEK data in June 2020. The damage probability is not equally distributed, but channels at the end of the Switcher ASIC (`SerOut` side) seem to be affected with higher likelihood [40].

5.2 Increase of HV Currents

Increasing high voltage currents were first observed in April 2020 in modules in +x direction (see figure 3.3(b)), where a higher level of beam backgrounds is expected [41].
When the accelerator is turned off, a discharge or annealing effect of the increased currents is visible in the KEK data. This recovery is amplified when the matrix is off, while the beam is still on.
Figure 5.3 shows the increase of HV current of module 1011 during the time between the 9th and 19th April 2020. At the end of this time frame the current value already exceeds −1 000 µA.

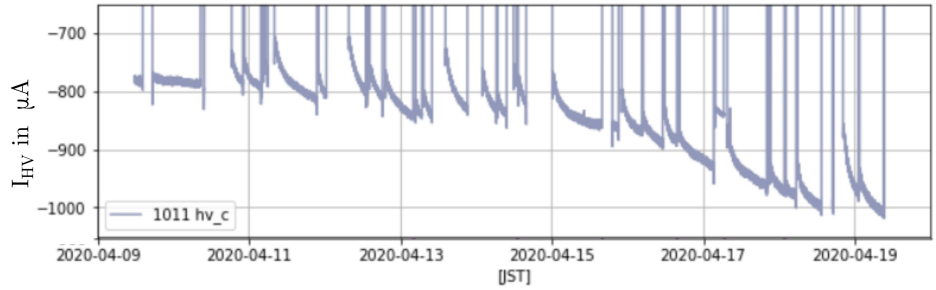

Figure 5.3: Increase of HV current for module 1011 between the 9th and 19th April 2020. With −1 000 µA the current is already close to the hard limit of −1 400 µA[41].

Since the HV channel of the LMU PS is limited to a supply of −1.4 mA current, further increasing currents could endanger the module operation.
When the current limit is reached, the set voltage can not be applied anymore. This would result in a drop of efficiency for the affected modules. Therefore, all power supplies were modified during the summer shutdown 2020, resulting in an increase of HV limits by a factor of two.
Nevertheless, the underlying mechanism has to be studied and understood. Therefore, measurements were performed during the latest irradiation campaign in September 2020 to test, if the behavior can be triggered by the MAMI electron beam.

CHAPTER 6

Irradiation at Mainz Microtron

To perform studies aimed at understanding the damage mechanism introduced in section 5.1, several irradiation campaigns were planned and executed at the Mainz Microtron (MAMI). This chapter unfolds the prerequisites and conditions for the measurements, that were carried out.

A short introduction of the MAMI accelerator is given in section 6.1.
Section 6.2 describes the experimental setup.

6.1 Irradiation Facility MAMI

The Mainz Microtron (MAMI) is an electron accelerator located at the Institute of Nuclear Physics at the University of Mainz. It consists of a normal-conducting linear accelerator (linac) and multiple levels of racetrack microtrons [42].
In the following, the operation principle will be shortly explained. For reasons of greater clarity, subsequent explanations will be restricted to acceleration steps, that precede the beam extraction on the device under test (DUT).
Figure 6.2 shows a site plan of the required pre-accelerators and the location of the measurement setup. It is a cutout of the complete floorplan for the MAMI irradiation facility and limited to the experimental halls A and B.

Unpolarized electrons are provided by a thermal source and pre-accelerated by an injector linac, achieving an output energy of 2.1 MeV [43]. This beam is then used as an input for a cascade of three so-called race track microtrons (RTM) [44].
A schematic illustration of the working principle is shown in figure 6.1.

The linear acceleration of electrons via microwave radiation is limited to energy gains in the order of $\sim$ MeV m^{-1} [45]. Therefore, a single linac structure is passed repeatedly exploiting the accelerating field on each pass.

Two D-shaped electromagnets are used deflect the accelerated electrons. Since increasing beam energies result in increased bending radii within the constant magnetic field, the track pattern reminds of ancient race tracks, giving the RTM its name [45]. To match the radio-frequency to the increasing

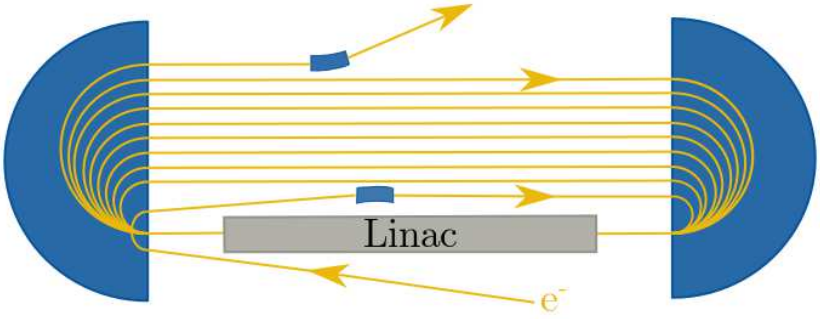

Figure 6.1:
Working principle of a race track microtron. Bending magnets are shown in blue. The electron beam is displayed in yellow. The electrons pass a single linac structure repeatedly.

path length and ensure the intended acceleration, the RTM's resonance condition has to be fulfilled. It is given by

$$n \cdot \lambda_{rf} = 2\pi \frac{\Delta E}{e \cdot c \cdot B} \quad , \tag{6.1}$$

where n is an integer, λ_{rf} the radio-wavelength of the cavity, ΔE the energy gain per pass-through and B the magnetic field of the bending magnets [46]. The increase in path length has to be an integer multiple of the radio-frequency wavelength.

With a maximum output energy of 855 MeV at a single magnet weight of 450 t, the third cascade step (MAMI-B / RTM3) exhausts the mechanical limits of the design, making it the world's biggest microtron [45].
The essential parameters of all three RTMs can be obtained from table 6.1.

		unit	RTM1	RTM2	RTM3
general	input energy	MeV	3.5	14	180
	output energy	MeV	14	180	855
	linac traversals	#	18	51	90
	year of commissioning		1979	1983	1990
magnets	flux density	T	0.10	0.56	1.28
	max. orbit diameter	m	0.97	2.17	4.43
	magnet distance	m	1.67	5.59	12.86
	weight of one magnet	t	1.3	43	450
r.f. system	number of klystrons	#	1	2	5
	linac length	m	0.80	3.55	8.87
	frequency	GHz	2.4495	2.4495	2.4495
	energy gain per pass	MeV	0.60	3.24	7.5

Table 6.1: Machine parameters of the RTM stages [47] [48].

The MAMI accelerator is normally operated in continuous wave (cw) mode, providing a continuous electron beam. To achieve prompt irradiation bursts, the electron source has to be triggered externally. By fast switching of the Wehnelt voltage for a predefined duration, the facility can be utilized for pulsed beam investigations. This working mode is called macro pulse mode.

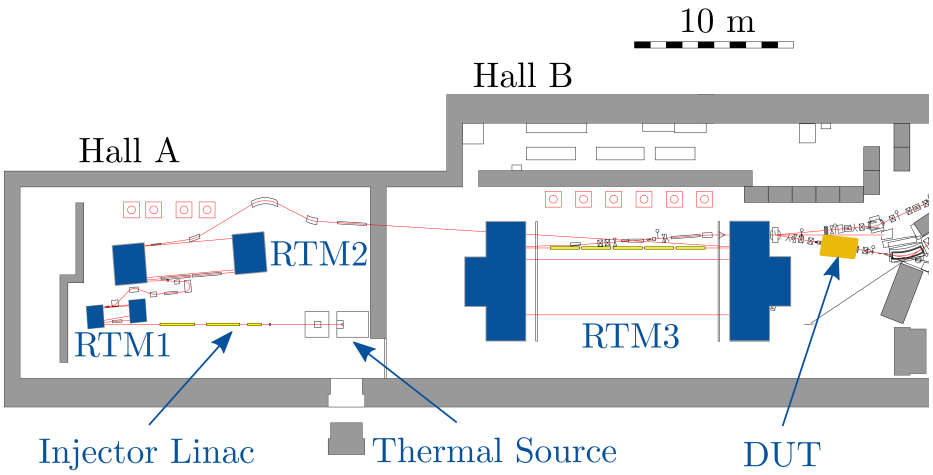

Figure 6.2: Floorplan of the MAMI accelerator. It consists of an injector linac with following cascade of three Race Track Microtrons (RTM) and provides an electron beam with an energy of 855 MeV[49].

6.2 Measurement Setup

The following section introduces the setup and measurement sequence, utilized to take data during triggered macro pulse injections. The setup mainly consists of the Hybrid5 laboratory setup, introduced in chapter 4.3.1 and illustrated in figure 4.6(b).

To allow additional triggering of the MAMI accelerator and synchronized readout of the matrix and more precise current information, the setup is expanded by further hardware. A scheme of the full setup is illustrated in figure 6.4.

The additional components are briefly introduced in the following.

Pulse Generator
A *Hewlett-Packard HP81104A Pulse Pattern Generator* allows triggering of MAMI macro pulses, while sending trigger signals to the Hybrid5 setup with a precise timing configuration. The programmed pulse pattern is illustrated in figure 6.3. With each measurement, the Hybrid5 system receives 41 pulses of 800 ns width and 180 µs total period. Each pulse is a negative square pulse with 0.5 V amplitude.
20 µs before the 21st Hybrid5 pulse, a single rectangular pulse triggers the accelerator's electron source, leading to a 40 µs irradiation burst on the DUT. To match the required Nuclear Instrumentation Module (NIM) logic standard of the control room, the MAMI pulse has a voltage level of −1.2 V for 800 ns.
The described pulse pattern is already optimized for the specific cable lengths and delays of the accelerator, which cause a time difference of 26.4 µs between trigger and beam arrival on target. This value was obtained by observing the MAMI trigger pulse together with the output signal of two scintillator plates, located at the beam extraction location. An oscilloscope picture is shown in A.1. The presented pulse pattern is used to record data of 20x4 raw frames before the injection, 1x4 raw frames during injection and 20x4 raw frames after beam injection. Therefore, it is possible to investigate changes in the matrix response, caused by irradiation bursts on the module.

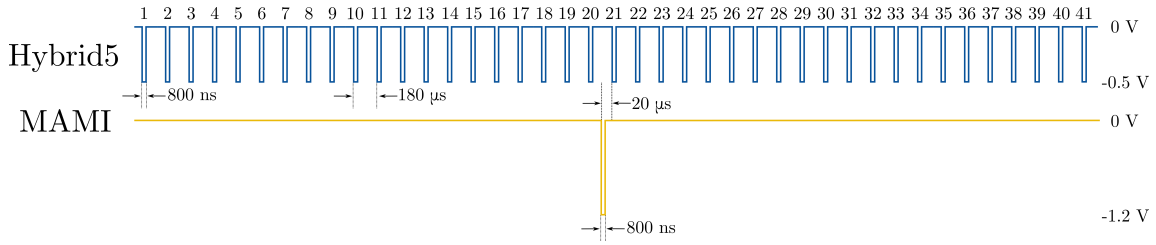

Figure 6.3: Scheme of the measurement pattern provided by the pulse generator. The Hybrid5 system is triggered 41 times, while the accelerator is triggered once. The arrangement of the trigger pattern results in data taking of 20x4 frames before, 1x4 frame during and 20x4 frames after the beam injetion.

Trigger Logic Unit
The *EUDET JRA1 Trigger Logic Unit* (TLU) generates the trigger for the Hybrid5 system from the pulse generator's pulses [50].
A built-in discriminator board produces output pulses of fixed length, if the threshold voltage is exceeded for more than 3 ns. These pulses are provided to the DHE where they are further processed for the module.

Motorstage
An X-Y table is installed at the beamline and offers the possibility to scan the DUT's surface. It is controlled via an EPICS IOC running on a Raspberry Pi so that the coordinates can be controlled via the network. With a stepsize of $\frac{1}{2000}$mm in horizontal and $\frac{1}{20000}$mm in vertical direction, module components can be scanned with sufficient spatial resolution. The resolution of the measurement is primarily restricted by the beam-size and accelerator stability.

External current monitoring
The LMU PS, that provides the Hybrid5 system with all required voltages, features current monitoring via built-in ADCs. Since the design is restricted to a sampling rate in the order of ~1 Hz, and current resolution is limited to 1 mA, external hardware is mandatory for high precision current measurements.
Keithley Sourcemeters/Multimeters are used to read out system currents at the Hybrid5 power cable with increased time and current resolution.
To achieve even higher sampling rates, the signals at the monitoring lines of the LMU PS ADC are picked up by two *Raspberry Pis* and additional *Waveshare ADS1256* 24-bit ADC boards. By multiplexing between the two to three connected input channels, a sampling rate of 230 Hz up to 360 Hz can be achieved. Due to the restricted input range of 0 to 5 V, Raspberry Pi and ADC board are extended by a stripboard, equipped with inverter circuits for singals of negative currents.
The LMU PS provides all system voltages from five flavors of regulator cards. A list of all 23 voltages and their corresponding domain can be found in A.2, together with a sketch of the powering scheme, including output potentials and standard values. Since those regulator cards do not share a common ground connection, simultaneous measurements of signals from different PS domains effectively short all grounds to net ground via the Raspberry power cable and the shielding of the ethernet cable.
To overcome this problem, the Raspberry Pis are operated with power supplies with floating outputs and unshielded network cables, resulting in a floating ground connection.
During the latest irradiation campaign in September 2020, the external current monitoring was further improved by using *Tektronix TDP1000* active differential probes on a *Tektronix MSO4104* oscilloscope with a sampling rate of 5 GS /s.

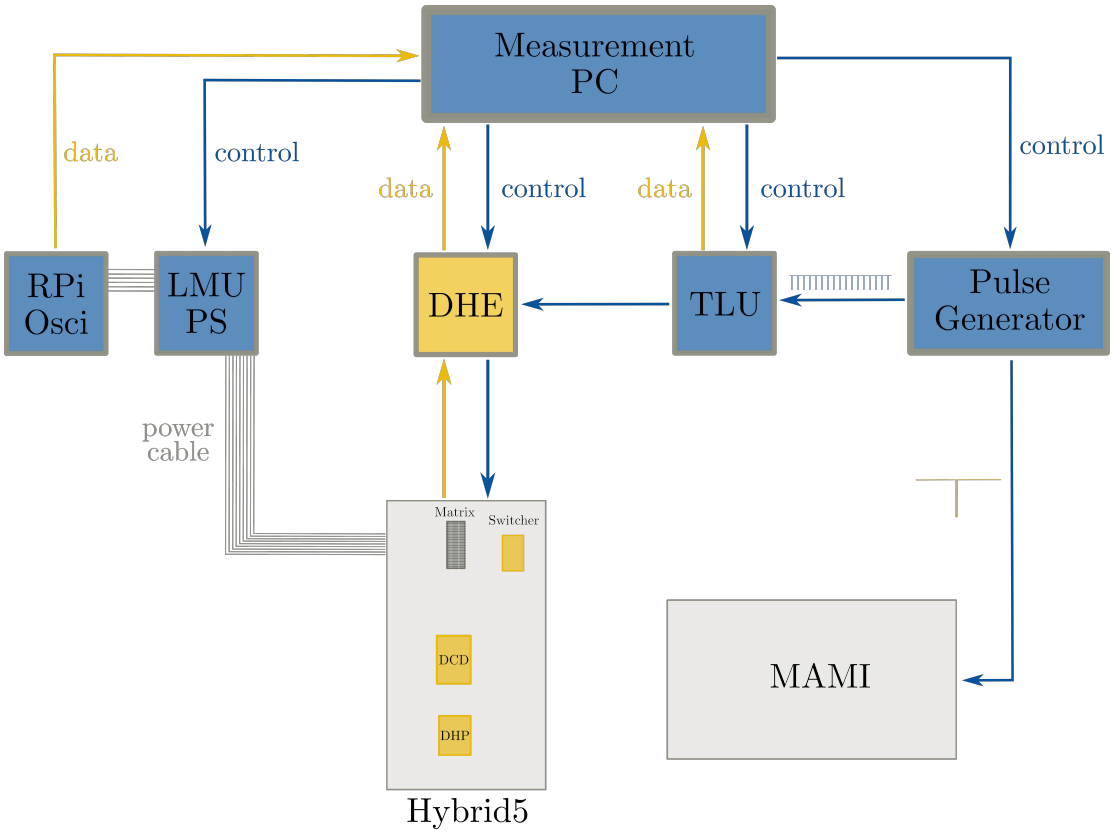

Figure 6.4: Schematic of the measurement setup. The Hybrid 5 setup that was introduced in section 4.3.1 is upgraded with additional hardware. Pulse generator, Trigger Logic Unit (TLU), an external current monitoring via Raspberri Pi (RPi) and oscilloscope are used to take data and control macro pulse injection.

CHAPTER 7

Irradiation Burst Studies

The results of the measurements, performed during three irradiation campaigns in November 2019, July 2020 and September 2020, are presented in this chapter.

Section 7.1 deals with the characterization of the irradiation setup. It describes the measurements of beam-size (7.1.1) and resulting effective dose on the device (7.1.2), that are important for the classification of the following studies. The performed measurements are sorted in chronological order.

Section 7.2.1 describes a coarse scan of the Hybrid5 module area. In section 7.2.2, the oscilloscope probing of resulting damaged Switcher output channels is discussed.

Section 7.3.1 shows the result of a fine scan of the Switcher ASIC area, while section 7.4.1 focusses on the effects of beam-pulse injection into the clear and gate regulators.

Finally, the option of a fast shutdown of module voltages is examined in terms of possible protection against future beam loss events at KEK in section 7.4.2.

7.1 Irradiation Setup

During the beam incident in July 2019, the accelerator lost 150 mA of beam current within 40 µs. The amount of beam current lost in the detector was extrapolated to an effective dose of 500 rad for the PXD modules. The total ionizing dose (TID) is a measure for cumulative damage within a material, caused by ionizing irradiation. It is also referred to as dose D and describes the amount of deposited energy $E_{\text{dep.}}$ by ionization per unit mass m.

$$D = \frac{E_{\text{dep.}}}{m} \tag{7.1}$$

The following two sections describe the measurements and calibrations, that are performed, to achieve an accurate reproduction of beam loss events with macro pulses at MAMI.

7.1.1 Beam Size Determination

To evaluate the accuracy of the performed scans and estimate the deposited dose, the beam size on the device has to be determined first.
Therefore, the beam is centered with low beam current in constant wave mode and data is recorded with a duration of 10 to 60 s.

The hitmap of each measurement is plotted together with a projection of the number of hits in vertical and horizontal direction. Assuming a normal-distributed beam, a Gaussian function is fitted to the data points [51].

$$f(x) = \frac{1}{\sigma\sqrt{2\pi}} \exp\left(\frac{-(x-\mu)^2}{2\sigma^2}\right) \tag{7.2}$$

From the obtained fit values and the matrix pixel size d_{pixel}, the full width at half maximum FWHM of the electron beam can be estimated in both dimensions [51].

$$\text{FWHM}_{\text{hor/ver}} \approx \sigma \cdot 2.355 \cdot d_{\text{hor/ver,pixel}} \tag{7.3}$$

Figure 7.1 shows the determination of the beam size for Hybrid H5031, with a pixel pitch of 50 µm x 70 µm.

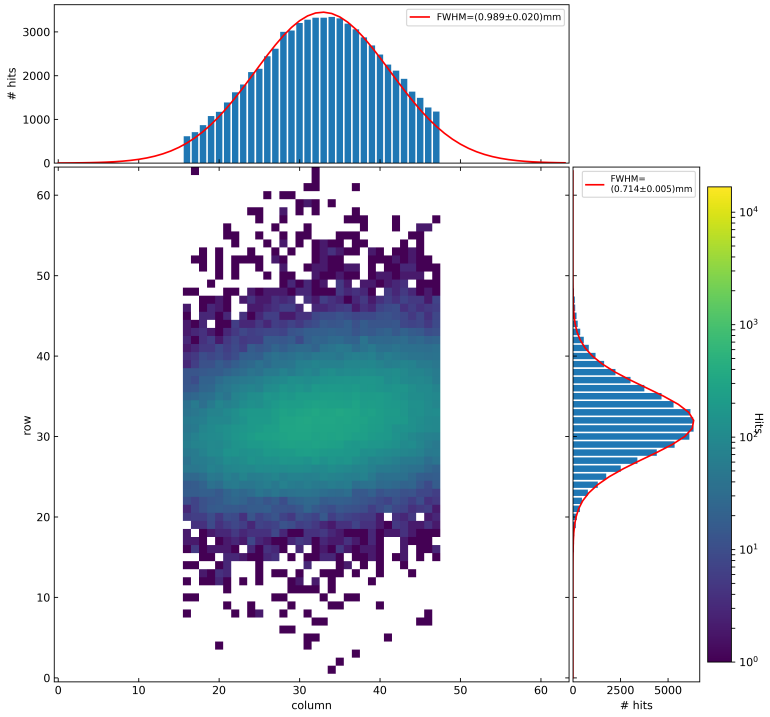

Figure 7.1: Determination of beam size on the device. The hitmap resulting from recorded scan data is plotted and a Gaussian function is fitted to the horizontal and vertical projection. From the fit values, the FWHM of the electron beam can be calculated with equation 7.3.

The resulting beam size at FWHM is

$$\mathrm{FWHM}_{\mathrm{hor}} = (0.989 \pm 0.020)\,\mathrm{mm} \qquad \mathrm{FWHM}_{\mathrm{ver}} = (0.714 \pm 0.005)\,\mathrm{mm}. \tag{7.4}$$

By repeating the procedure for two Hybrid5 modules in total 16 times, the mean beam size is calculated to be

$$\overline{\mathrm{FWHM}}_{\mathrm{hor}} = (0.970 \pm 0.024)\,\mathrm{mm} \qquad \overline{\mathrm{FWHM}}_{\mathrm{ver}} = (0.733 \pm 0.012)\,\mathrm{mm}. \tag{7.5}$$

A table of the values obtained from the individual measurements can be found in A.3.

7.1.2 Dose Injection Estimation

The effective dose, deposited by the electron beam is dependent on energy, beam current, area, pulse length and target material. While the beam energy is fixed to 855 MeV, macro burst length is 40 µs and the beam size can be measured, some calibration constants have to be calculated, to compute the effective dose per pulse.
To achieve a comparable deposition of 500 rad within 40 µs, the required dose rate $\dot{D}_{\mathrm{req}}$ is

$$\dot{D}_{\mathrm{req}} = \frac{500\,\mathrm{rad}}{40\,\mu\mathrm{s}} = 12.5\,\mathrm{Mrad/s}. \tag{7.6}$$

The dose rate of the electron beam with current I_{beam}, area πr^2_{beam} and stopping power $P^{\mathrm{Si}}_{\mathrm{stop}}$ in silicon is defined as[1]

$$\dot{D}_{\mathrm{beam}} = P^{\mathrm{Si}}_{\mathrm{stop}}\,(855\,\mathrm{MeV}) \cdot \frac{I_{\mathrm{beam}}}{e \cdot \pi r^2_{\mathrm{beam}}}. \tag{7.7}$$

Tabulated data from the National Institute of Standards and Technology (NIST) webpage [52] is utilized to determine the collision stopping power of 855 MeV electrons in silicon. From figure 7.2

$$P^{\mathrm{Si}}_{\mathrm{stop}} = 2.087\,\mathrm{MeV\,cm^2\,g^{-1}} \tag{7.8}$$

is obtained.
Here, the unit of $P^{\mathrm{Si}}_{\mathrm{stop}}$ is $\mathrm{MeV\,g^{-1}\,s^{-1}}$ which can be expressed via the more commonly-used rad = $1 \times 10^{-2}\,\mathrm{J\,kg^{-1}}$ using

$$\mathrm{MeV\,g^{-1}} = 1.602 \times 10^{-14}\,\mathrm{Mrad}. \tag{7.9}$$

Equation (7.7) can then directly be given in Mrad/s via

$$\dot{D}'_{\mathrm{beam}} = 1.602 \times 10^{-14} \cdot P^{\mathrm{Si}}_{\mathrm{stop}}\,(855\,\mathrm{MeV}) \cdot \frac{I_{\mathrm{beam}}}{e \cdot \pi r^2_{\mathrm{beam}}}. \tag{7.10}$$

An additional correction factor is the area ratio of the beam intensity profile compared to an ideal square signal. It is needed to get an estimate for the effective dose per pulse and takes beam losses in the accelerator into account.

[1] Note that this property (assuming homogeneous density) is independent of the thickness of the device since dose is normalized to the mass and the mass increases with the same rate as the thickness.

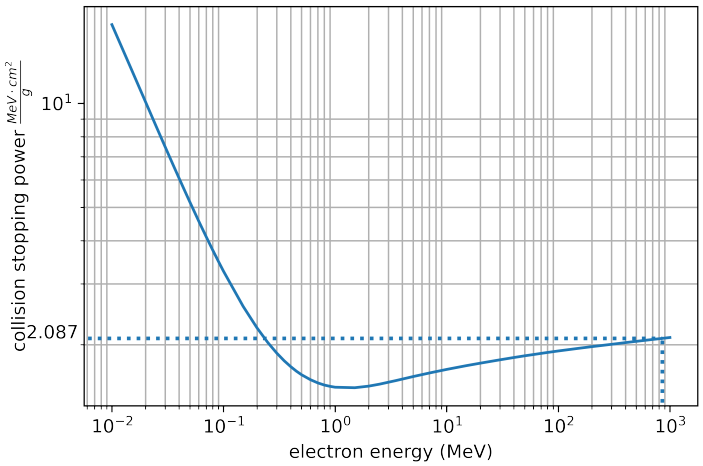

Figure 7.2: Collision stopping power of electrons in silicon. The horizontal and vertical dotted lines mark the value of 2.087 MeV cm^2 g^{-1} for 855 MeV electrons.

Two scintillation counters are located behind the DUT to measure the intensity profile of the electron beam. Loss factors are estimated by analyzing the scintillator traces on the oscilloscope for increasing beam currents. Figure 7.3 shows the calculation of the area ratio for a beam current of 10 µA.

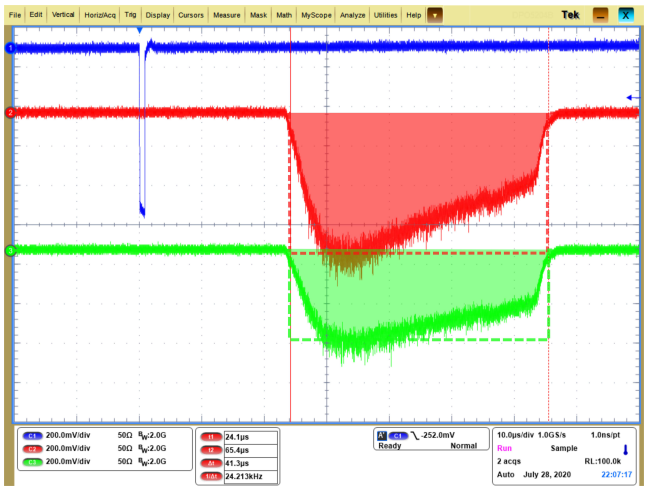

Figure 7.3: Determination of the area ratio as correction factor for beam losses in the accelerator. The blue signal shows the MAMI trigger pulse. In red and green signals of two scintillators located behind the DUT are shown. The area under the beam intensity profile is compared to an ideal rectangular shape (dashed lines) to calculate the correction factor.

The oscilloscope screenshots for 1 µA, 2.5 µA, 5 µA, 7 µA and 10 µA can be found in A.4.
Figure 7.4 shows the resulting effective dose factor, depending on the beam current. The effective dose at FWHM can also be determined by equation 7.10. Therefore, the fraction of the beam current within FWHM I^*_{beam} is calculated by integrating the Gaussian beam distribution between $-r^*_{\text{beam}}$ and

r^*_{beam}. These values are taken as quadratic mean from the beam size calculated in equation 7.5. The effective dose at FWHM is shown as a dotted red curve, while the blue line indicates the area ratio, that represents beam loss effects. The data points are linearly interpolated to get an estimate over the whole current range.
In order to imitate the beam loss event at KEK as closely as possible, the beam current was set to 1 µA for most of the following measurements, leading to a comparable deposited dose.

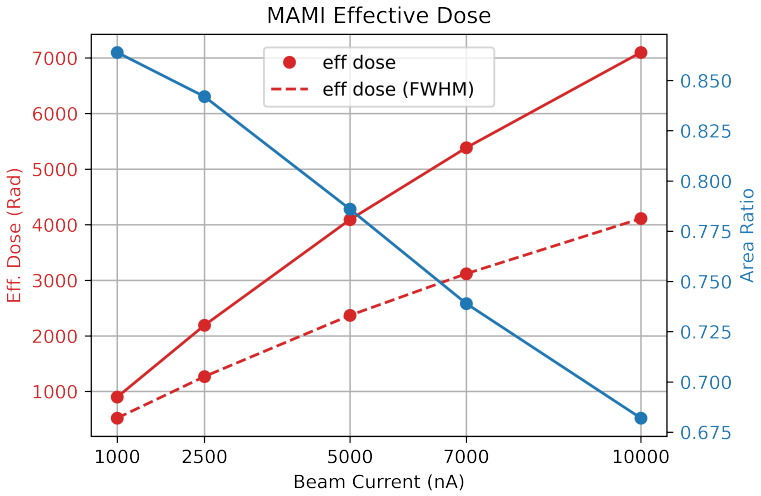

Figure 7.4: Effective dose per pulse. The solid red line shows the effective dose of a 40 µs macro pulse of 855 MeV electrons for different beam currents. The red dashed line specifies the dose within the FWHM. It is calculated with the values of equation 7.5. The blue line illustrates the area ratio of the beam intensity profile compared to an ideal rectangular pulse. It decreases with higher losses for increasing beam currents.

7.2 Hybrid5 Module Irradiation

7.2.1 Coarse Module Scan

During a first irradiation campaign in September 2019, the damage mechanism, that leads to inefficiencies in single quadruple rows, is investigated.
Although the occurrence in rows of four hint to a damage of the Switcher ASIC, it can not be excluded, that the vulnerable region lies within the matrix or its surroundings.

Therefore, different points on the matrix, Switcher and interspace between them are irradiated with pulse trains of 20 macro pulse injections each. Single injections are separated by a time difference of 700 ms.
A specific pattern of irradiation points is followed, while stepwise increasing the beam current from 4 nA up to 800 nA. The sensor is installed further away from the beam exit window (~70 cm) than for the measurement presented in 7.1.1 during this first campaign. Therefore, an increased beam spot of 1.2 cm FWHM is measured and the dose estimation varies for the following measurements.

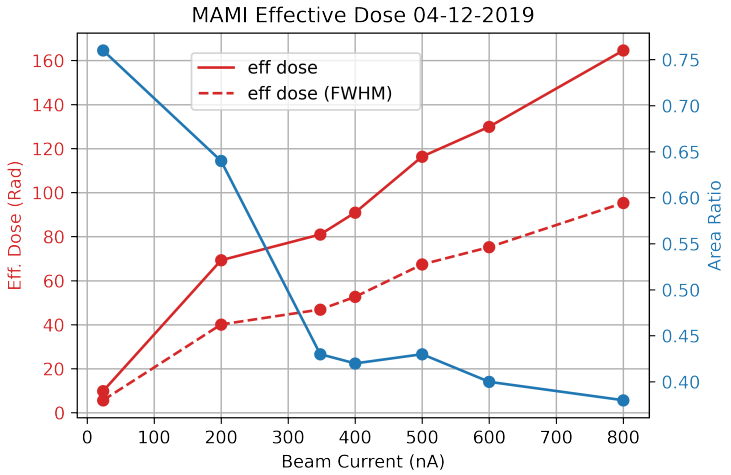

Figure 7.5: Effective dose per pulse during the first irradiation campaign in 2019. The effective dose is clearly reduced due to the the increased beam spot and unexpectedly high beam losses in the accelerator (see A.4).

In addition, unexpectedly high beam-loading losses (see A.4) result in a reduced effective dose, for the measurements presented in this chapter, especially for high beam currents.
Figure 7.5 shows the effective dose, dependent on the beam current for the campaign end of 2019. Even with the highest chosen beam current of 800 nA, the intended dose of 500 rad is missed by a factor of five at FWHM.
In addition to measurement points on and around the matrix, six irradiation points are distributed over the Switcher area with a mutual distance of 1 mm (see figure 7.6). For orientation on the module, the beam is centered on the matrix (P0) in constant wave mode, before switching to macro pulsed mode for irradiation.

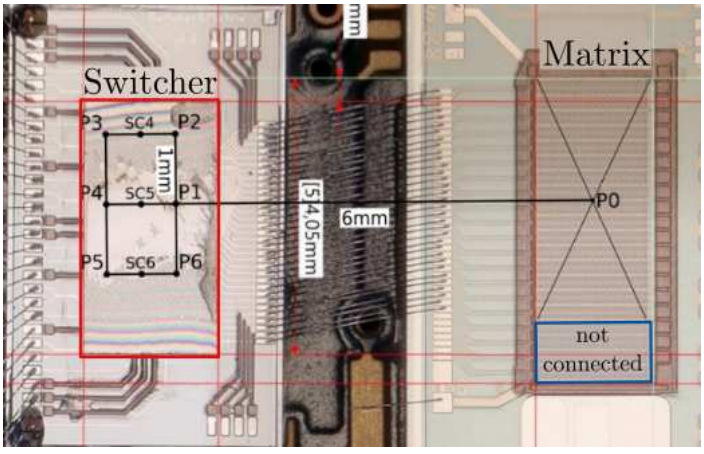

Figure 7.6: Irradiation points on the Switcher area. The beam is centered on the matrix in point P0 to know the exact position of each irradiation point on the Switcher (P1-P6). Due to unconnected first 16 matrix rows, the irradiation grid is not centered on the ASIC (red square).

Due to unintentional misalignment caused by the unconnected last four matrix quadruple rows (see figure 7.6), the irradiation pattern is not perfectly centered on the Switcher, but slightly shifted upwards. Measurement points P1 - P6 are irradiated counter clockwise for increasing beam currents from 4 nA up to 800 nA and 20 consecutive pulse trains per setting.

Hybrid H5027

During the pulse injections into the DEPFET matrix and surroundings, no changes are observed in Switcher currents or the matrix response for Hybrid H5027. The irradiation of the Switcher area does not yield any changes in the module behavior up to a beam current of 300 nA.
With consecutive measurements at $I_{\text{beam}} = 500\,\text{nA}$ on point P5, increases in Switcher currents can be observed with the external Raspberry Pi monitoring (see 6.2). The current behavior during the 20 injections is shown in figure 7.7. With the first macro pulse, ClearOn and ClearOff absolute currents are increased from 14 to 19 mA and −10 to −16 mA, respectively.
These are the values, set as current limits within the power supply software. By increasing the limits and allowing more current to flow, stable module operation can be restored.

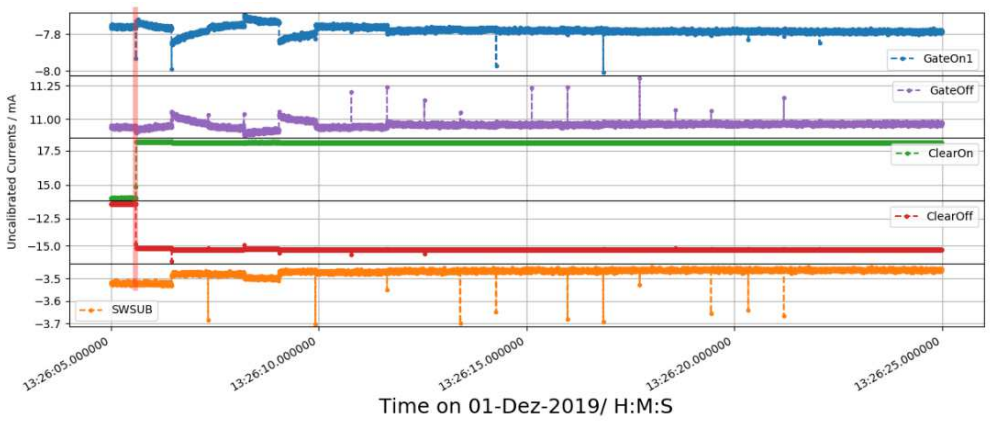

Figure 7.7: Injection series on point P5 with increased Clear currents, recorded by the Raspberry Pi system. The first injection is marked with a red line.

As depicted in figure 7.8, consecutive irradiation of point P5 confirms the observation of a vulnerable spot in the lower left corner of the Switcher ASIC.
The increase of currents now also affects the remaining monitored Switcher currents.

During the irradiation of point P5, also temporary changes in the response of single matrix quadruple rows are observed. Figure 7.9 shows the 41 raw data frames recorded during one macro pulse injection on P5. Raw frame 1 is subtracted from each of the following frames, which improves the visibility of small changes under the assumption of stable pedestal values. The electron beam is arriving within the 21st frame and clearly visible in the data. A single matrix quadruple row shows reduced signal during and shortly after the irradiation. Since the damage is not permanent, the observations from KEK can not be fully reproduced yet.

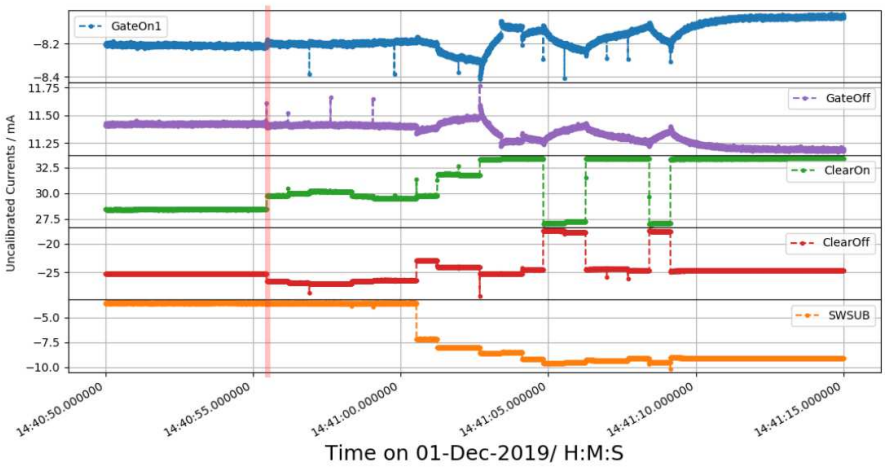

Figure 7.8: Injection series on point P5 with increased Clear currents, recorded by the Raspberry Pi system. The first injection is marked with a red line. Since already figure 7.7 showed changes in Switcher currents on this point, P5 is confirmed as vulnerable spot.

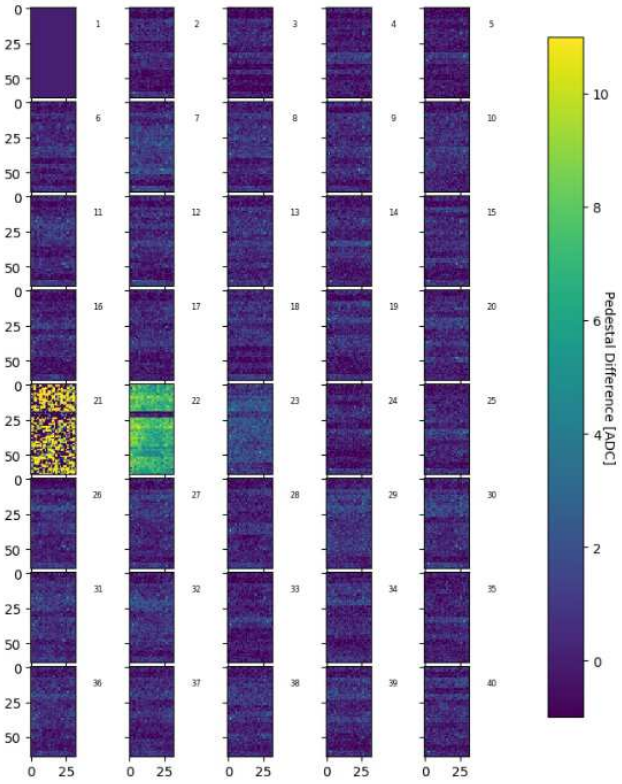

Figure 7.9: Matrix response during beam injection on point P5. The difference of frame i and frame 1 is plotted for all 41 frames during irradiation. A single matrix quadruple row shows a different response during the injection but is not permanently damaged.

With a more finely-spaced irradiation pattern in the lower right corner (see 7.10(a)), the observed behavior can not be reproduced. While no effects are visible during injections on points P6.1 to P6.3, irreparable damage is induced with the first measurement on point P6.4.
As shown in table 7.1 and figure 7.10(b), the module can not be operated after the incident. Even with a current limit of 70 mA for ClearOn, nominal operation voltages can not be achieved anymore. The additional clear current seems to flow in between the ClearOn and ClearOff channel. Therefore, both nets and the respective potentials seem connected.

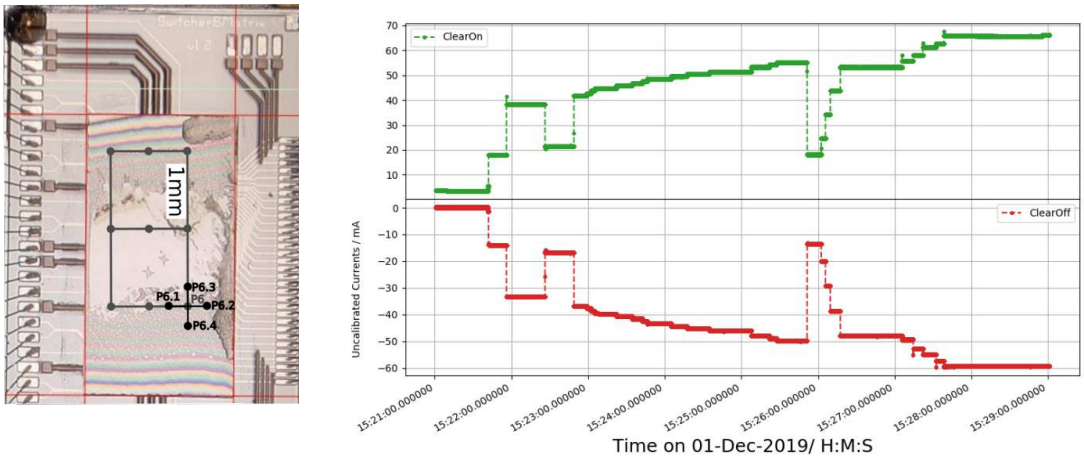

(a) (b)

Figure 7.10: (a) Photograph of the Switcher ASIC with marked injection grid of the lower right corner. (b) Clear current behavior after the destructive measurement on point P6.4. At 70 mA, ClearOn and ClearOff still seem to be connected and the module can not be operated anymore.

	nominal		after incident (in current limit)	
	I in mA	U in V	I in mA	U in V
ClearOn	8	19	70	19
ClearOff	-7	3	-64	16

Table 7.1: Clear currents and voltages after the destructive measurement on point P6.4 of H5027.

Hybrid H5028

To confirm the observations, the study is repeated with Hybrid H5028. It has the same matrix size and bonding scheme as H5027. Therefore, the misalignment of the measurement grid is the same as depicted in 7.6. With multiple measurements on points P3, P4 and P5, no changes are observed with the Raspberry Pi current monitoring. The destructive behavior of irradiating point P6.4. can not be reproduced entirely. With 217 additional injection series at 800 nA beam current, only five measurements result in an increase of clear currents ($\Delta I_{\text{clear}} \approx 25\,\text{mA}$). The module stays fully functional with adjusted current limits.

First Conclusion

Although permanent changes in the occupancy of single matrix quadruple rows could not be provoked during this measurement, the increase of Switcher currents was reproduced.
The external current monitoring (see 6.2), provided by the Raspberry Pis, improves the understanding of the module behavior during irradiation bursts. However, the sampling rate is still not sufficient to resolve single injections of 40 µs.
Even though the observations were not fully reproducible, lower left (P5) and lower right (P6) corner of the Switcher ASIC were identified as susceptible regions.

7.2.2 Oscilloscope Probing of Damaged Switcher Channels

To investigate the damage, that occurred on H5028 and led to the observed increased currents, the first five clear and gate output channels of the Switcher are probed with the oscilloscope. A surfboard, wirebonded to the corresponding pads, allows the pickup of output signals and further processing via pin headers.

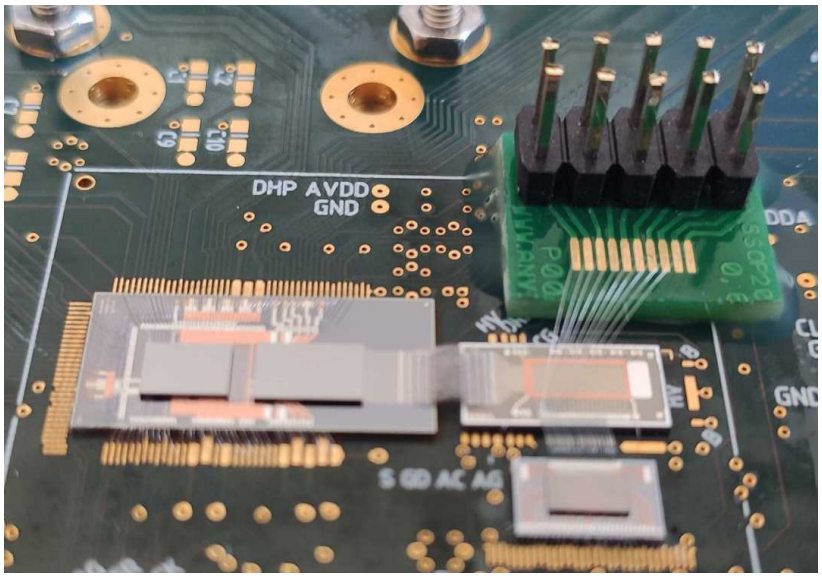

Figure 7.11: Photograph of H5028 with additional surfboard, that allows probing of the first 5 Switcher output channels. Wirebonds are connecting the additional board and the Switcher outputs.

During nominal operation, the swrefin voltage is kept at $V_{\text{swrefin}} = -5\,200\,\text{mV}$, resulting in a Switcher reference voltage of $V_{\text{swrefin}} - V_{\text{swsub}} = 1.8\,\text{V}$. The behavior of the Switcher outputs and resulting matrix response is also studied for varying V_{swrefin} in figure 7.13.

Results

Already at the nominal operation voltages, one of the five measured Switcher output channels shows a different behavior.
Figure 7.12 shows the oscilloscope data of clear and gate output channel 0, which looks equivalent to the signals of channel 1,2 and 4. The signals of the clear pulse (blue) and gate pulse (red) match the expectation of the normal readout procedure of one DEPFET quadruple row.

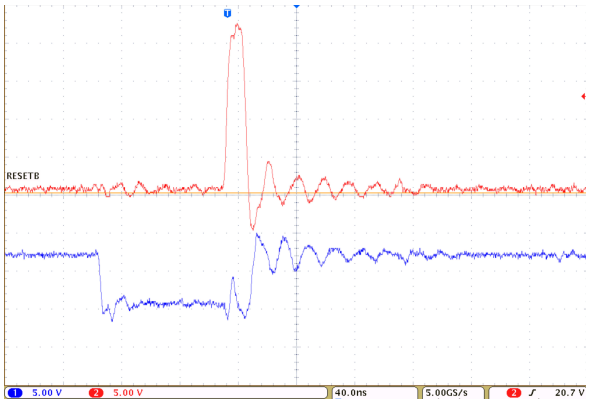

Figure 7.12: Output signals of Switcher channel 0 at default operation voltages recorded with the oscilloscope. The clear pulse is shown in red, while the blue line indicates the gate pulse.

Within 100 µs, the involved pixels are activated by applying the negative gate voltage, the signal is sampled and the charge in the internal gate is cleared by applying the positive clear pulse.
Clear channel 3 (figure 7.13(a)), that corresponds to the matrix rows 12 to 15, exhibits a behavior, deviating from the regular pulse shape. The decay time of the associated pulse is significantly increased.

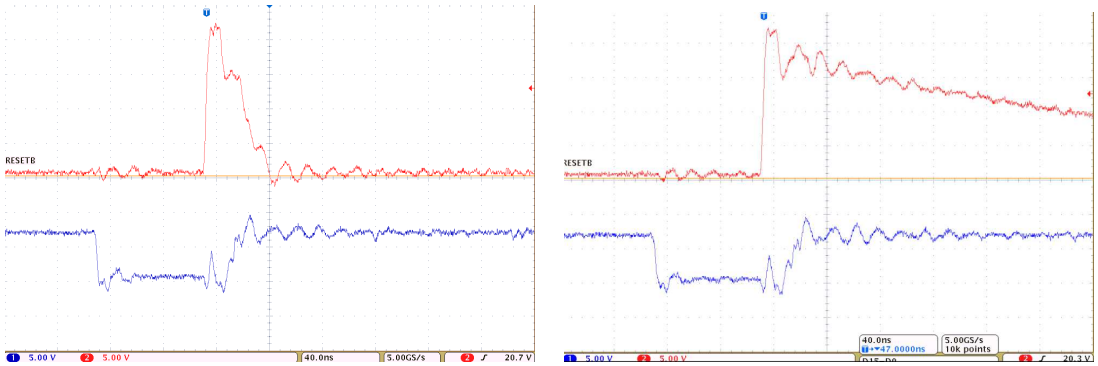

(a) (b)

Figure 7.13: (a) Output signals of the damaged Switcher channel 3 at default operation voltages. The clear pulse is shown in red, while the blue line indicates the gate pulse. The decay time of the Clear signal is significantly increased. (b) Output signals of the same Switcher channel at reduced $V_{\text{swrefin}} = -5\,600\,\text{mV}$. The decay time is even further increased.

When lowering the digital voltage of the Switcher by decreasing the Swsubin voltage, the decay time of the clear pulse increases even further. Figure 7.13(b) shows an example for $V_{\text{swrefin}} = -5\,600\,\text{mV}$. By setting $V_{\text{swrefin}} = -5\,700\,\text{mV}$, the damaged Switcher channel gets also visible in pedestal data. Figure 7.14 shows the pedestal difference for Hybrid H5028 for the voltages $V_{\text{swrefin}} = -5\,700\,\text{mV}$ and $V_{\text{swrefin}} = -5\,200\,\text{mV}$. The damaged output channel results in a corrupted readout of pixel data in the matrix rows 12 to 15.

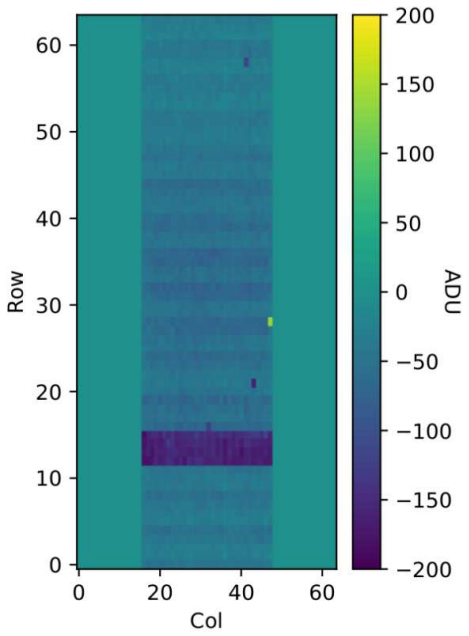

Figure 7.14: Pedestal difference of H5028 with visible damaged Switcher channel. Pedestals taken with $V_{\text{swrefin}} = -5\,200\,\text{mV}$ are subtracted from pedestal data taken with $V_{\text{swrefin}} = -5\,700\,\text{mV}$. Only the matrix rows 12 to 15 show a changed behavior with lower pedestal values for decreased V_{swrefin}.

7.3 Switcher ASIC Irradiation

7.3.1 Fine ASIC Scan

To confirm and delimit the vulnerable regions of the Switcher, a fine scan of the ASIC area is performed during a second irradiation campaign in July 2020 with Hybrid H5029.
The measurement principle and setup are not changed, except for the beam current and repetition rate. Since the possibility of inducing damage is already confirmed from the last campaign, the number of injections per measurement is reduced from 20 to 1. The beam current is increased to 2.5 µA for the following measurements, in which the Switcher area is scanned in a three-column scheme.

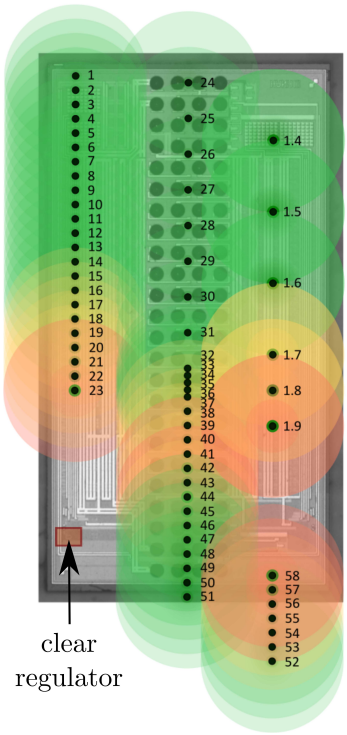

Figure 7.15: Heatmap of Switcher scan. Circle diameters correspond to 1 mm FWHM. Green circles represent measurements with no effect. Yellow circles indicate measurements with single injection peaks, while red circles describe measurement that provoked permanent damage.

Results

Figure 7.15 shows a heatmap resulting from the finer scan of the Switcher area. The photograph shows the bottom side of the ASIC, overlayed with circles that indicate the measurement points and observations. Each circle has a diameter of 1 mm, which translates to the estimated FWHM of the electron beam at the device. The measurement points are color-coded in green, yellow and red. Green circles represent measurements with no effect on the module operation. Yellow circles indicate macro pulse injections that led to single injection peaks in the Switcher currents, but no permanent increases. Permanent damages, e.g. increased currents or inefficient matrix quadruple rows, are represented by red circles.

From the distribution over the Switcher area, the results from 7.2.1 can be confirmed. The vulnerable regions are located in the lower left and lower right corner of the Switcher. This is the side, where the `SerOut` signal can be provided to a daisy-chained Switcher.
Figure 7.15 also shows the location of the clear regulator, that generates the internal voltages `ClearHIGH` and `ClearLOW` (see 4.1). The gate regulator is located in the opposite lower corner. According to the chip designer, both regulators are vulnerable under high instantaneous radiation [53].

After the fine scan, the results are verified by irradiating a second module on the clear regulator. The beam current is set to 1 µA with one injection per measurement.

The previous used modules H5027, H5028 and H5029 can only connect the first 16 of 32 Switcher channels to the matrix, since they are assembled with an 16-channel Switcher adapter. For this study, Hybrid H5012 is used. It is equipped with a 32-channel Switcher adapter. Therefore, it is possible to wirebond the 16x4 matrix rows to the last 16 of total 32 Switcher channels. This allows the direct observation of the Switcher channels at the `SerOut` side, which show a higher damage probability in the KEK data (see5.2).
With the first injection on the clear regulator, the result of the fine scan can be confirmed. Also the observation of inefficient quadruple rows can be reconstructed for the first time. Figure 7.16 shows a difference plot of raw data during the injection. Each of the recorded raw frames is subtracted from the first frame of the measurement to increase the visibility of small changes in the signal response. For clarity, the plot is restricted to the frames 16 to 30. The damage in the second to last Switcher channel can be precisely traced back to the incoming macro pulse in frame 20.

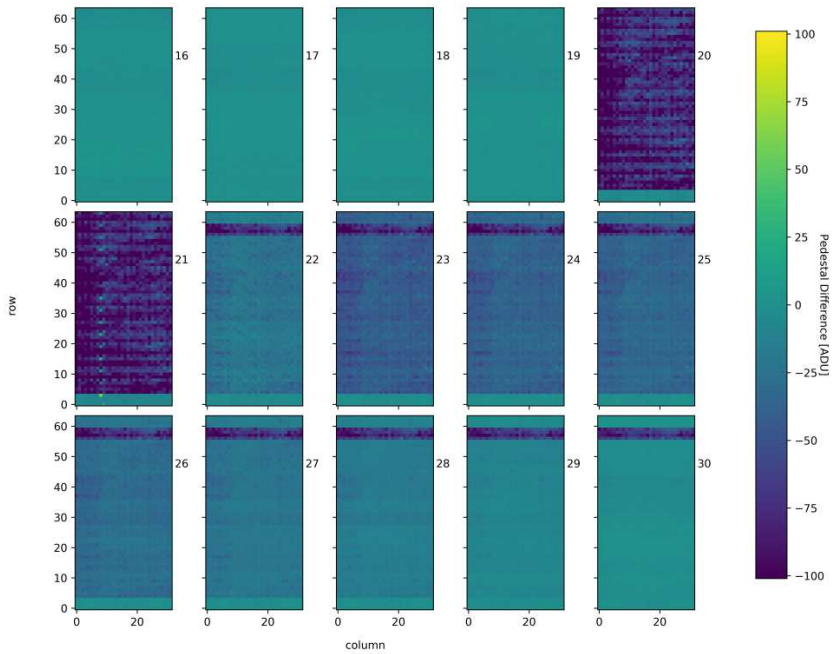

Figure 7.16: Raw data difference of 15 raw frames during injection. The first raw frame is subtracted from each following frame, which improves the visibility of small changes. During the injection, frame 20 shows corrupted data for one readout cycle, leading to universally lowered signal. Ten frames after the injection all but one quadruple row returned to their initial signal response. The second to last Switcher channel is damaged permanently.

The inefficiency is still persistent after the measurement and also shows reduced pedestal values (see figure 7.17) and distorted response in a source scan with low energy electron beam in cw mode (see figure 7.18).
Together with the observation of recovered Switcher channels in later measurements, the damage pattern of the PXD modules (5) is now reconstructed in this irradiation burst study.
The loss of efficiency is traced back to the voltage regulators of the Switcher ASIC and can be reproduced reliably.

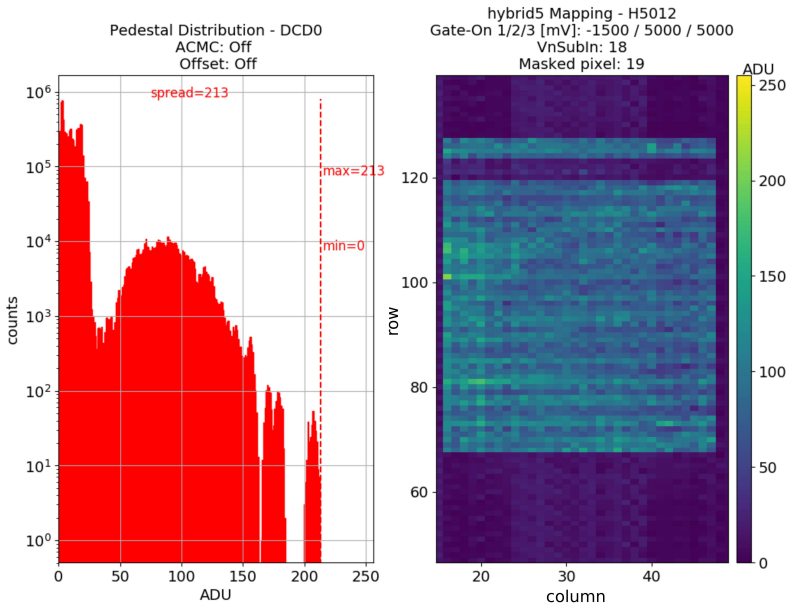

Figure 7.17: Pedestal values of H5012 after macro pulse injection on the clear regulator. The left histogram shows the pedestal distribution. A 192 gate Switcher sequence is used to imitate KEK operation. Since only Switcher channels 17 to 32 are connected to the matrix, the majority of unconnected pixels show low ADU values. On the right plot the pedestal map is shown. Due to the bonding scheme, connected matrix rows are plotted with the row numbers 64 to 127. This was accounted for in figures 7.16 and 7.18, where the same matrix rows are mapped to the row numbers 0 to 64. The second to last quadruple row shows reduced pedestal values.

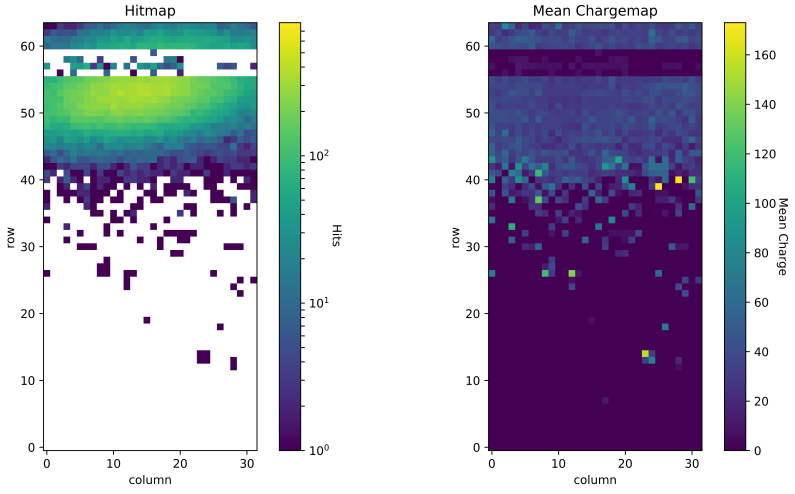

Figure 7.18: Source scan data with the damaged second to last quadruple row. A 10 s source scan is performed with the low intensity electron beam in constant wave mode. The beam is focussed on the second to last quadruple row. The matrix rows connected to the damaged Switcher channel show reduced signal in the hitmap (left) and also mean chargemap (right).

7.4 Test of Protective Measures

7.4.1 Switcher Voltage Threshold Scan

A third irradiation campaign is carried out at MAMI, to gain more information and test possible protective measures.
For the measurements presented in the following sections, a threshold scan is performed of the `ClearHIGH` and `GateHIGH` voltages. Starting with only applying the ASIC voltages (module in STANDBY), the respective voltage regulator is irradiated with single macro pulses of 1 µA beam current. With no applied voltages, the regulator should not be sensitive to prompt irradiation. The measurement procedure is repeated in steps of $\Delta V = 500$ to 1 000 mV to obtain voltage boundaries for a safe module operation.
To resolve the changes also during the 40 µs injection the external current readout is upgraded to the oscilloscope readout introduced in chapter 6.2.

Gate Voltage Study

Figure 7.19 shows the behavior of gate currents during the irradiation of the clear voltage regulator for `GateHIGH` voltages up to the standard value of 5 V. As expected, no current increases or damages are observed, when the clear regulator is not supplied with voltage.
Figure 7.20 shows the same measurement of Switcher currents, but this time the gate voltage regulator is irradiated. When the `GateHIGH` voltage is applied, current changes are measured that hint to a current flow between GateOff and SwSub during the time of injection. These current changes are pulse shaped and coincide with the timing of the 40 µs irradiation burst. The amplitude of the current pulses increase with increasing `GateHIGH` voltage. At $V_{\mathrm{GateOff}} = 3\,500$ mV, a permanent increase by 2.7 mA is observed for the GateOff current, while I_{SwSub} is decreased by 2.7 mA.

Clear Voltage Study

In figure 7.21, the behavior of Switcher currents for different `ClearHIGH` voltages during single irradiation bursts on the clear regulator is shown. The irradiation-induced current seems to flow between ClearOn and SwSub and increases with increasing `ClearHIGH` voltage.

During all of the measurements, the current limits of the LMU PS are increased (> 100 mA) to avoid unwanted voltage dependencies, if a current reaches the limit. If the current limit is reached, the regulator can not supply the target voltage anymore. The standard current limits prevent the currents from flowing freely in the corresponding domain, where they could potentially lead to harmful states for the module. By accident, the measurement at 3 000 mV is performed with the regular limits of $I_{\mathrm{lim,ClearOn}} = 18$ mA and $I_{\mathrm{lim,ClearOff}} = 14$ mA. Therefore, I_{ClearOn} is limited to 18 mA for roughly 100 µs and does not recover to its initial value.
The comparison of Switcher currents before and after this injection is shown in table 7.2. As already observed in earlier studies, the change of current balances among the different channels. This leads to the assumption that the additional current might flow in between the affected Switcher channels.

At $V_{\mathrm{ClearOn}} = 3\,500$ mV, an additional current flow between ClearOff and ClearOn can be obseved, before permanent damage of the last switcher channel is induced at $V_{\mathrm{ClearOn}} = 4\,000$ mV.

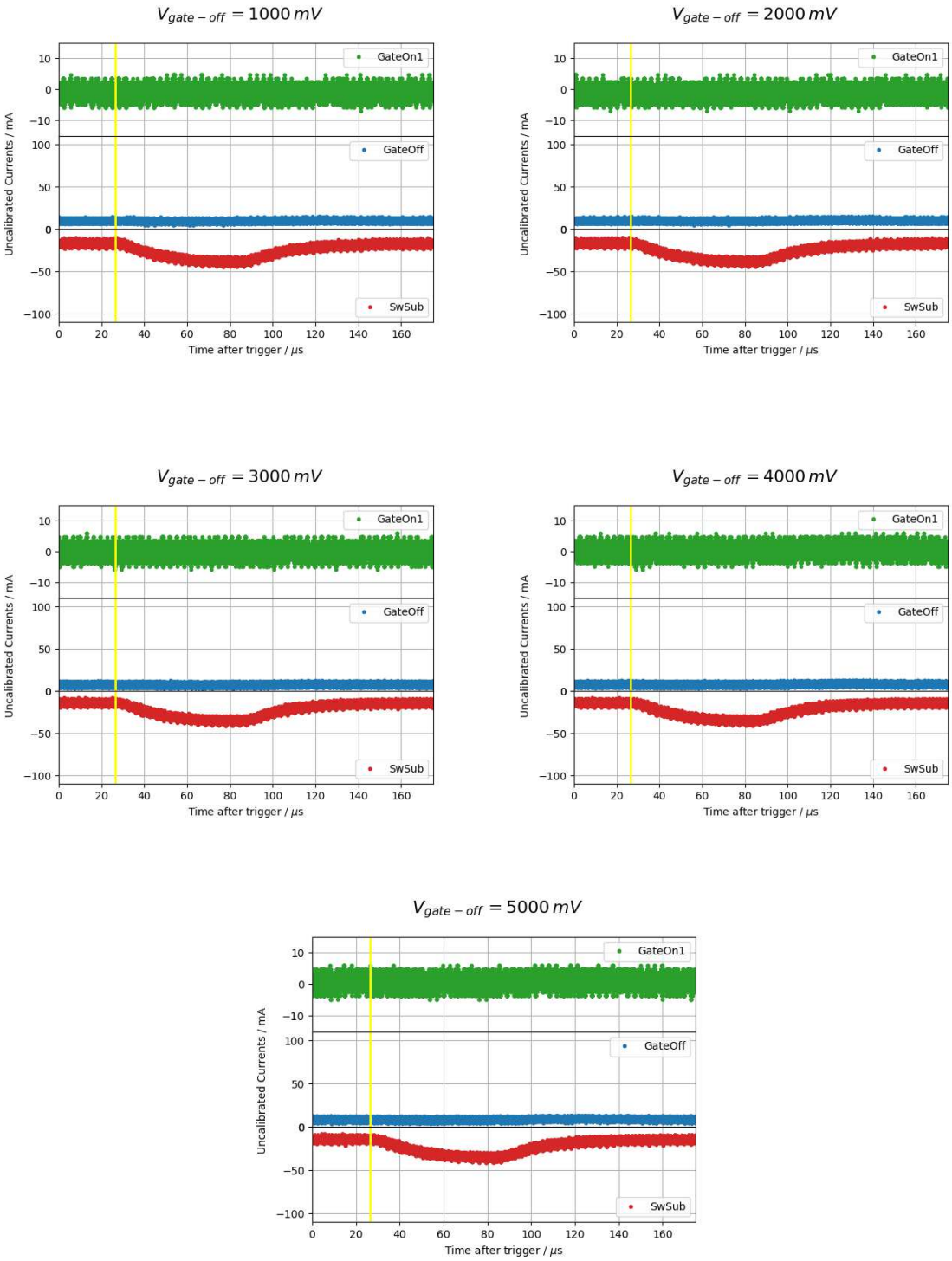

Figure 7.19: Irradiation on clear regulator with varying `GateHIGH` voltages. The currents of the Switcher channels GateOn, GateOff and SwSub are measured with an oscilloscope and active differential probes . The signals are picked off at the sensing circuit of the LMU PS internal ADC as voltages. A first calibration is done by calculating the corresponding current values from the schematics. The obtained values are plotted as 'Uncalibrated Currents' against time after the MAMI trigger. The beam arrives at 26.4 µs indicated by a vertical yellow line.

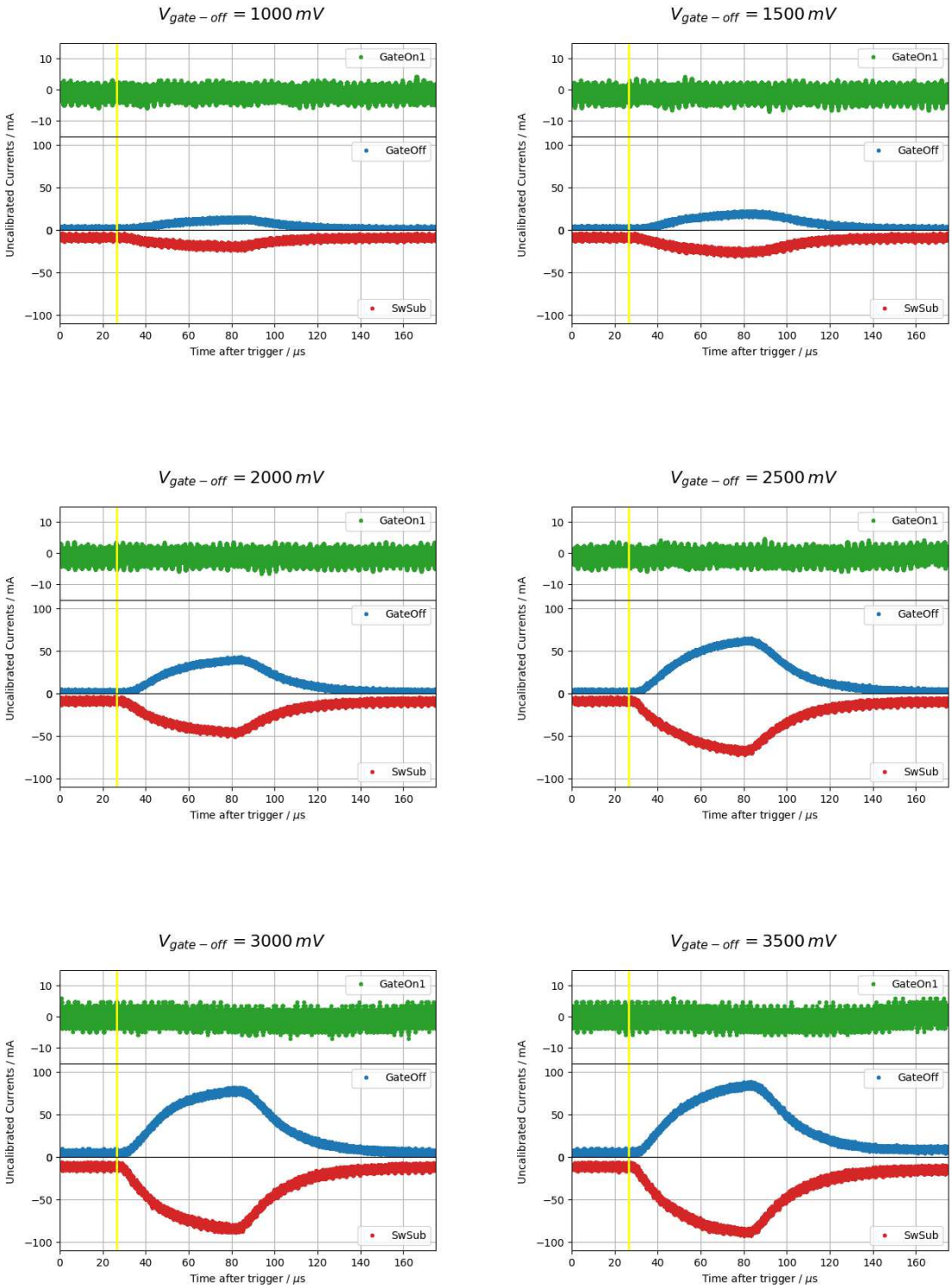

Figure 7.20: Irradiation on gate regulator with varying `GateHIGH` voltages. During the 40 µs irradiation burst, starting at the vertical yellow line, a change in GateOff and Swsub currents is observed. The amplitude of both current pulses increases equally with increasing `GateHIGH` voltage. This is consistent with the assumption of the additional current flowing in between the two channels.

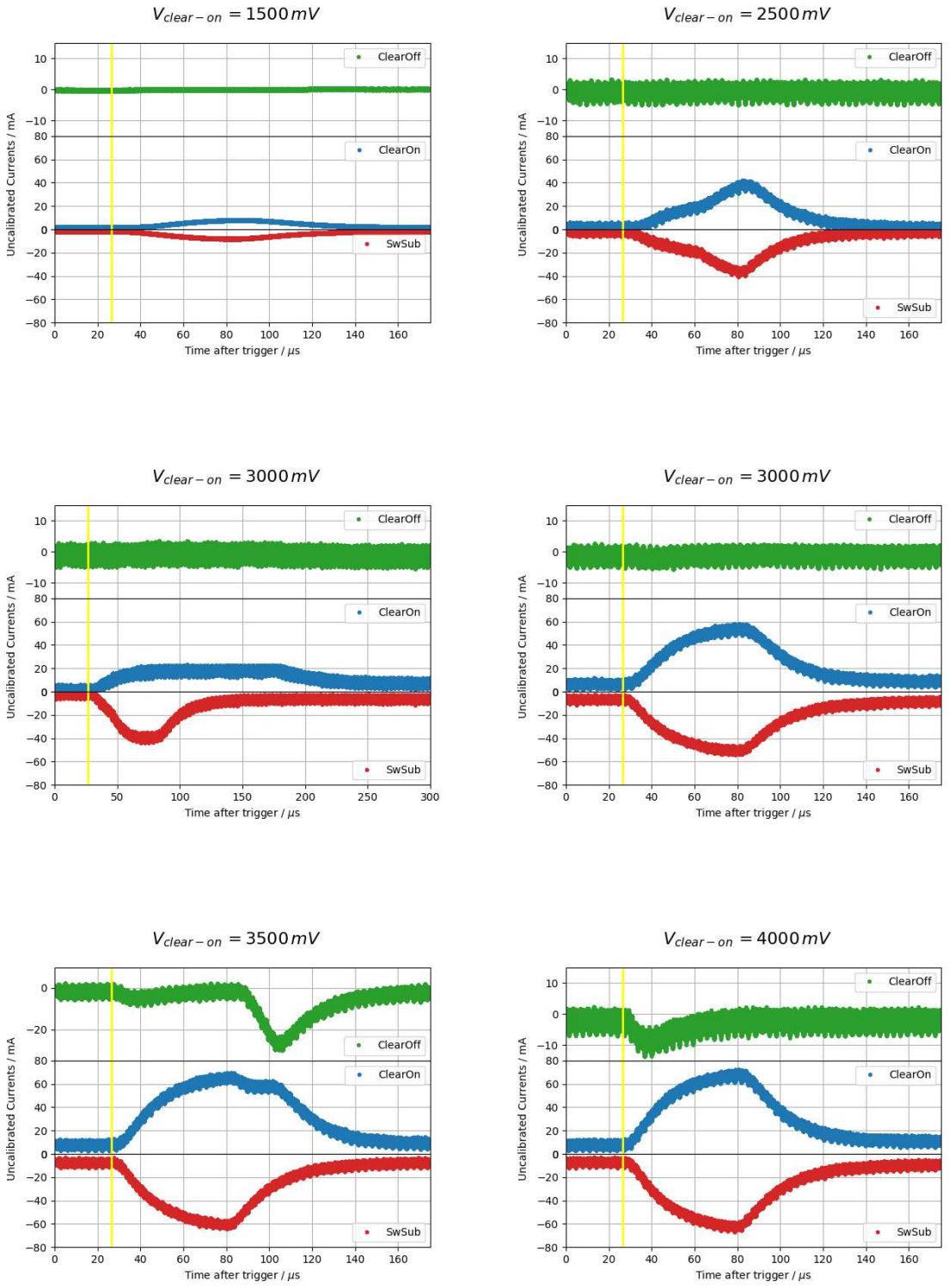

Figure 7.21: Irradiation on clear regulator with varying `ClearHIGH` voltages. At a threshold voltage of 3.5 additional current seems to flow in between the ClearOff and ClearOn channel. As also visible in 7.20, the voltage regulators of the Switcher seem prone to prompt irradiation burst, when the associated voltage is applied.

	before	after	ΔI
I_{ClearOn}	3.2 mA	8.2 mA	5.0 mA
I_{ClearOff}	−1.8 mA	−2.4 mA	−0.6 mA
I_{SwSub}	−2.4 mA	−6.8 mA	−4.4 mA
			$\Sigma\,(\Delta I_i) = 0\,\text{mA}$

Table 7.2: Comparison of Switcher currents before and after destructive irradiation on the clear regulator.

The irradiation of the gate regulator with only the `ClearHIGH` voltage applied confirms the observation of chapter 7.4.1. When each regulator is not supplied with its respective voltage, no radiation-induced currents are measured.

As a first conclusion, the module seems safe in STANDBY and it is possible to clearly differentiate between the two regulators. Currents in the clear channel of the Switcher are only visible during irradiation of the clear regulator. This observation is made analogously with the gate currents and the gate regulator. The threshold voltage, where the regulators are sensitive to prompt irradiation, is already reached at 3.5 to 4 V. Since nominal operation values are $V_{\text{ClearOn}} = 19\,\text{V}$ and $V_{\text{ClearOff}} = 5\,\text{V}$, reduced clear and gate voltages can not protect the module, while maintaining the DEPFET operation.

7.4.2 Fast Emergency Shutdown

As previous measurements confirmed the Switcher to be insensitive to irradiation in STANDBY, a fast shutdown of supply voltages could protect the ASIC.
To test this option, an additional pulse generator is used to trigger the interlock signal of the LMU PS with precise timing. The interlock trigger initiates the emergency shutdown of the LMU PS and all regulators are shut down. For the study, a modified version of the power supply is used that powers down the digital voltages 130 µs after receiving the interlock to maintain ASIC operation during the shutdown.

The programmable pattern of the pulse generator allows a variable delay between triggering the interlock and beam arrival at the DUT. Starting with large negative delays, the system is powered down before the beam arrives at the device. By decreasing the delay setting in steps, a critical value for the required beam-loss detection time can be obtained. At the experiment at KEK, fast diamond signals do provide a similar interlock signal.
Figure 7.22 shows the measurements, where the shutdown is initiated 3.5 to 0.5 ms before the macro pulse arrives at the Switcher. Measured clear and swsub currents are plotted together with the signal of the interlock signal. When the voltage at the interlock drops from 5 V to 0 V, the emergency shutdown is initiated. The shutdown can be observed as changes in the Switcher currents during the discharge of the module. With the delay setting of the first four measurements (figure 7.22), the discharge is already completed when the irradiation burst hits the Switcher (yellow vertical line). Therefore, these measurements are comparable to irradiations in OFF state. The impact of the irradiation bursts are not visible in the current monitoring and they do not lead to any damage.

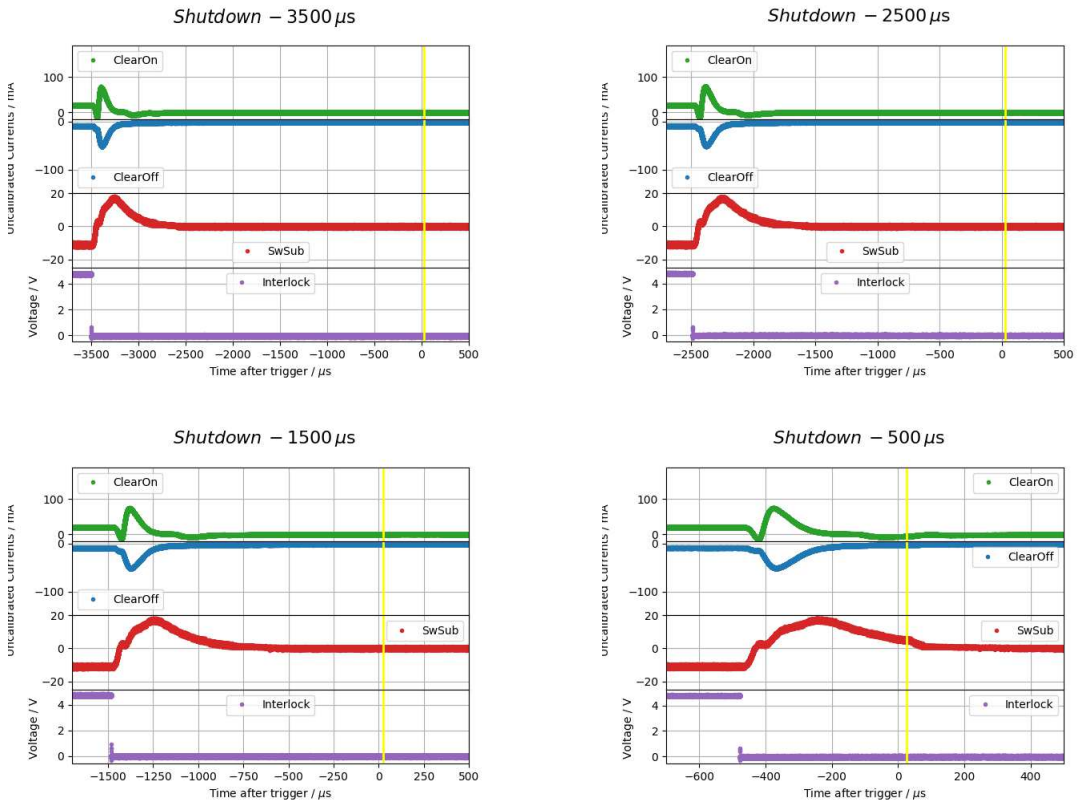

Figure 7.22: Shutdown study with delays between −3.5 and −0.5 ms. The bottom graph shows the triggering of the interlock signal. The MAMI accelerator is triggered at 0 µs, leading to the delayed beam injection at 26 µs (yellow vertical line). Any changes in the Switcher currents can be obtained from the top three graphs. The pulses shortly after the interlock signal correspond to the discharge of the module.

Figure 7.23 shows the measurement with further decreased time difference between shutdown and injection. Already at $\Delta t = -250\,\mu s$, the impact of the macropulse is visible in the Switcher currents. For lower delay settings, the injection pulse merges with the shutdown pulse and leads to increased amplitudes during the ramp down of voltages. The evolution of pulse height for the last five measurements is shown in figure 7.24. Due to a wrong vertical scale adjustment of the oscilloscope range, the ClearOn signal is cut-off at 74 mA for $\Delta t = -50\,\mu s$.

Already at $\Delta t = -10\,\mu s$, increased currents lead to heavy damage in the Switcher. A comparison of currents before and after the measurement are shown in table 7.3. Even if a beam loss event could be predicted 10 µs in advance, the emergency shutdown in this current form, is still not fast enough to protect the Switcher[2].

[2] This conclusion is only valid for the tested circumstances of 855 MeV electrons with 1 µA beam current and a 40 µs irradiation burst directly placed on the susceptible regulator of the Switcher ASIC

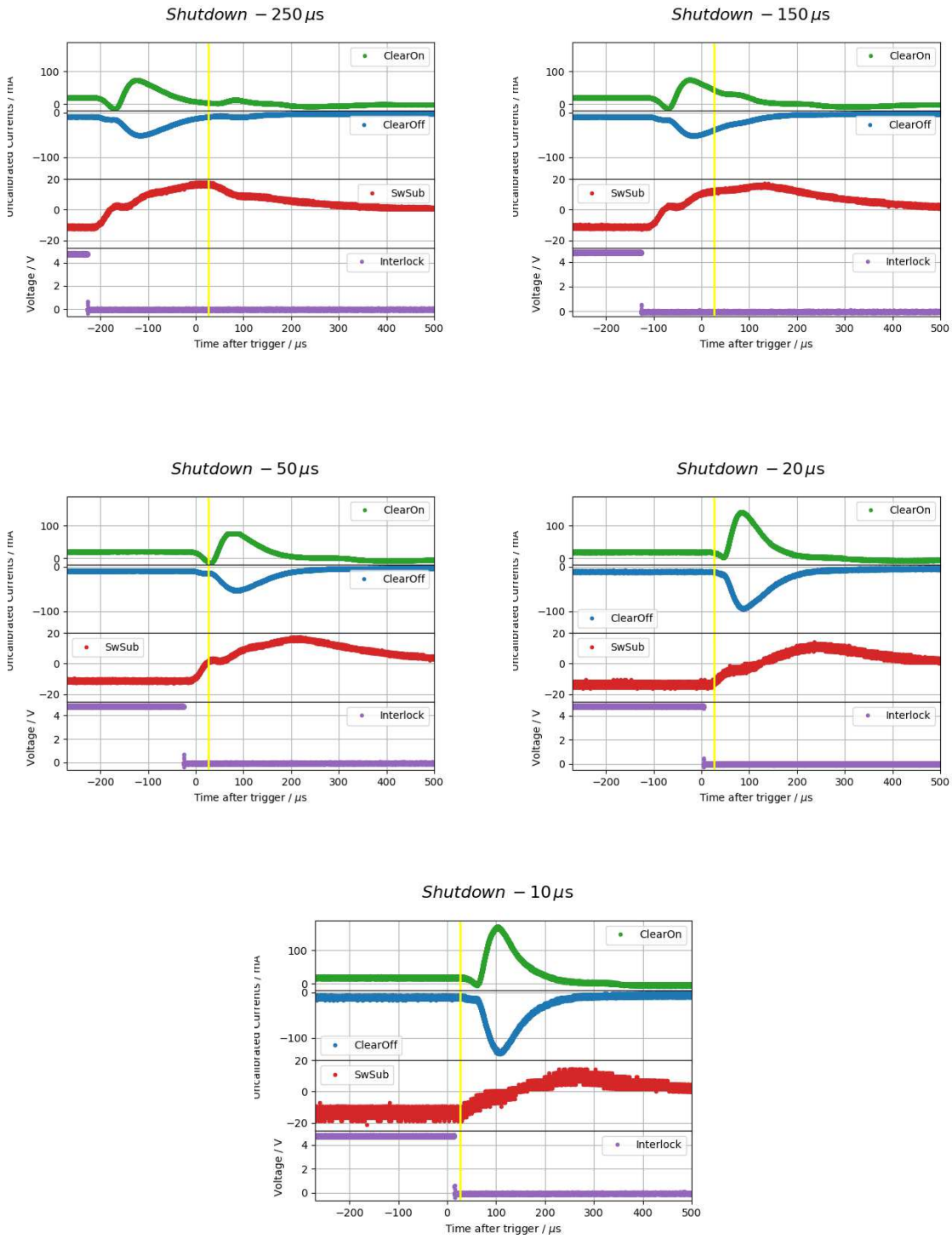

Figure 7.23: Shutdown study with delays between −250 and −10 µs. Already at $\Delta t = -250\,\mu s$ the pulse is injected during the discharge of the module. Shutdown pulse and injection pulse merge with decreasing time intervals between interlock and irradiation burst. As depicted in figure 7.24, this leads to increasing current changes in ClearOn and ClearOff. The measurement with $\Delta t = -10\,\mu s$ introduces permanent damage. The increased Switcher currents are displayed in table 7.3.

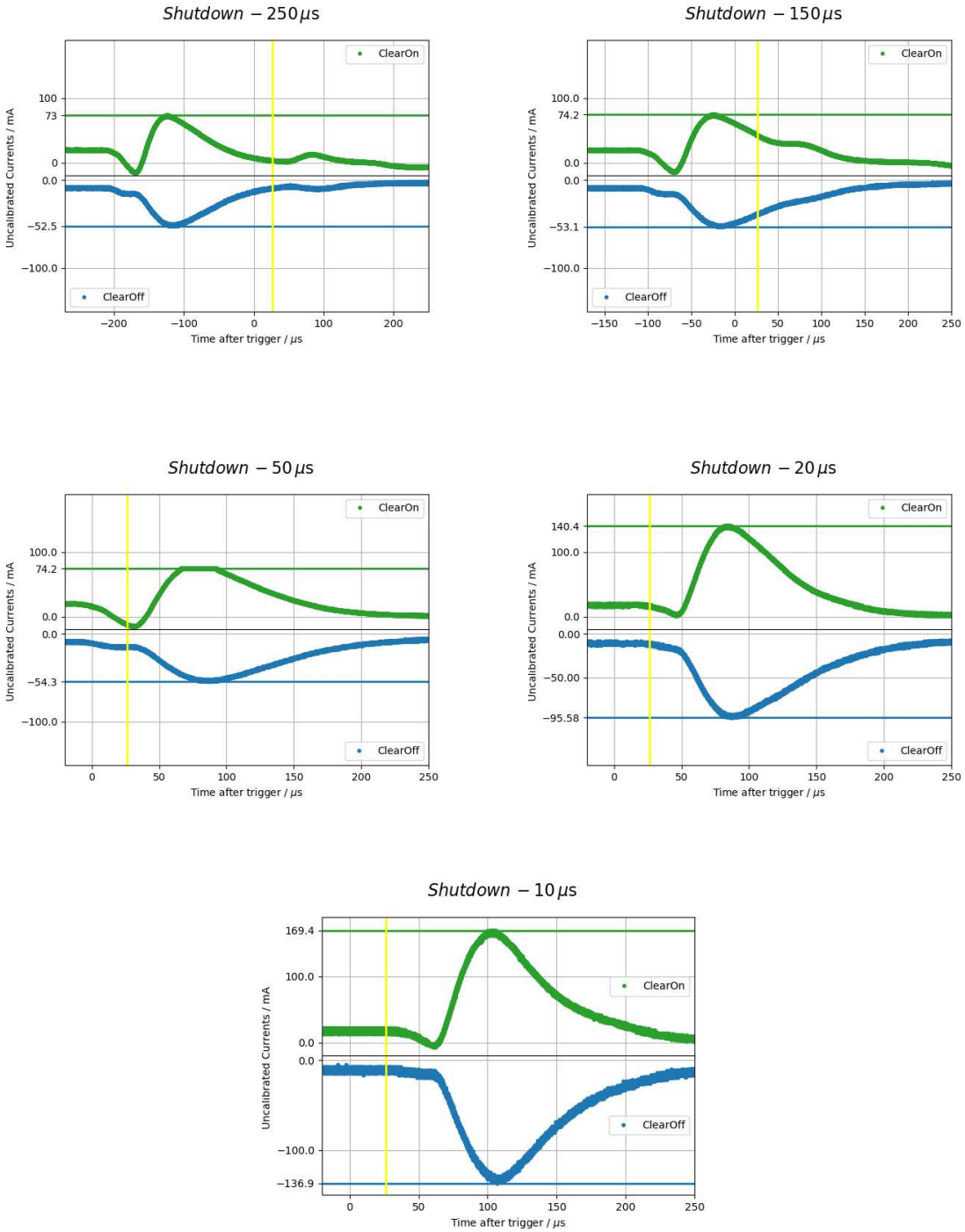

Figure 7.24: Evolution of pulse heights for decreasing delay setting in the shutdown study. At $\Delta t = -250\,\mu s$ shutdown and injection pulse can still be distinguished. The beam injection only shows a small influence on the Switcher currents. With decreased time interval between shutdown and injection, both pulses merge, leading to increasing current changes during irradiation. At $\Delta t = -50\,\mu s$, permanent damage is introduced. Due to a wrong vertical scale adjustment of the oscilloscope range, the ClearOn signal is cut-off at 74 mA for $\Delta t = -50\,\mu s$.

	before	after
SwSub	−11 mA	−15 mA
ClearOn	20 mA	102 mA
ClearOff	−9 mA	−84 mA
GateOn	−2 mA	−2 mA
GateOff	3 mA	4 mA

Table 7.3: Comparison of Switcher currents before and after destructive irradiation during the shutdown study with $\Delta t = -10\,\mu s$.

Although the current changes are not completely balanced between the different Switcher channels in this example ($\Sigma\,(\Delta I_i) = 4\,mA$), a similar distribution is visible. Together with the observation of equally increasing current changes in these channels during beam injection (see figure 7.24), this might be the main evidence to describe the effects within the Switcher ASIC. In the current understanding the electron could generate a photocurrent within a diode of a highvoltage transistor in the voltage regulators. However, the full damage mechanism is not reconstructed yet.

7.5 HV Current Increase

To reconstruct the HV current increase, that is introduced in section 5.2, multiple irradiation points are located on the matrix and the surrounding structures. An irradiation of the matrix center does not yield any changes in the high voltage current. Figure 7.25 shows further irradiation points on the matrix boundary. During beam injection HV and bulk current of the module are monitored with Keithley Source Measure Units (SMUs), which are connected directly to the Hybrid5 power cable.

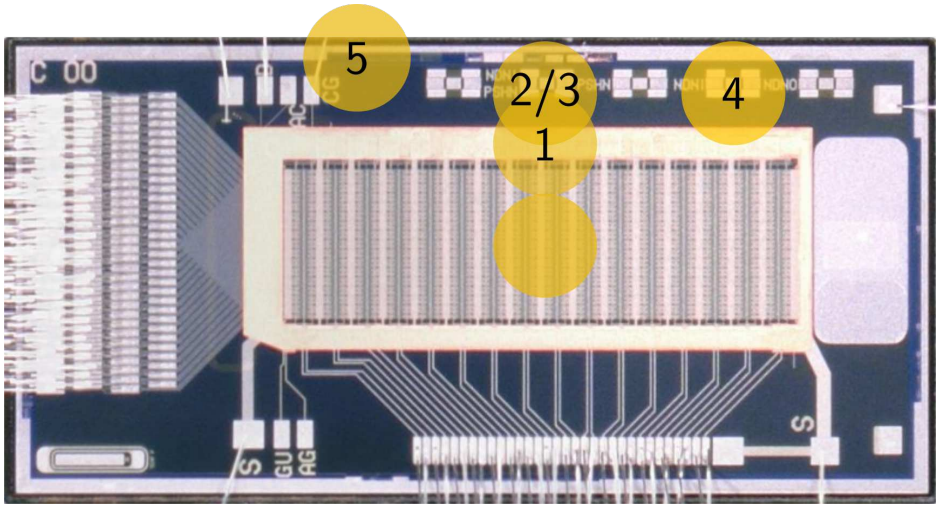

Figure 7.25: Irradiation points of Hybrid H5025 during the HV current study. The matrix boundary is irradiated with pulse trains of 1 to 1000 injections with a beam current between 1 µA and 10 µA.

During the irradiation of the matrix boundary the observation from KEK can be reconstructed. Figure 7.26 shows the response of bulk and HV current to multiple irradiation series on measurement points 1 to 5.

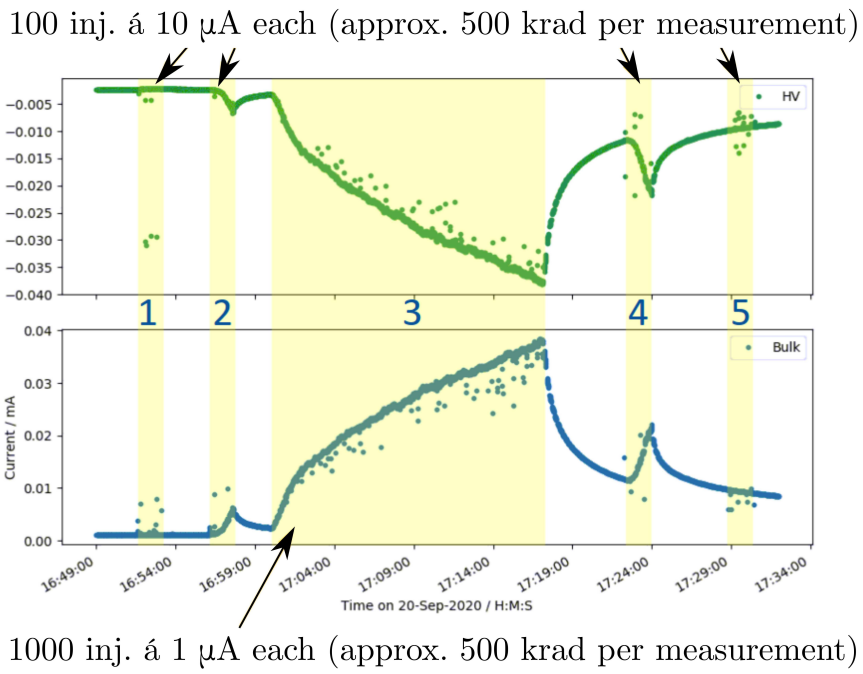

Figure 7.26: HV and bulk current increase during irradiation of the matrix boundary.

The signal response shows an irradiation induced increase of currents and the characteristic discharge behavior, when the beam is off. Since the measurement does not show any effect during irradiation of the matrix itself it might not be radiation damage. Although the mechanism is not fully reconstructed yet, charge-up effects that lead to avalanches at the backside structure are considered as potential cause.
An additional x-ray campaign is planned for beginning of 2021 to further investigate these observations.

CHAPTER 8

Summary and Outlook

Damages of the PXD modules, that have been observed after beam loss events at the accelerator in Japan, were investigated at the Mainz Microtron.
During a coarse scan of a demonstrator system, the Switcher ASIC turned out to be a vulnerable component under prompt irradiation.
In a finer scan of the Switcher area, the damage pattern of affected PXD modules was reconstructed. Inefficiencies of single matrix quadruple rows can be provoked by burst irradiation of the Switcher. The loss of efficiency could be shown to correlate to radiation bursts into the area of the voltage regulators for clear and gate voltages.
With the first detailed monitoring of system currents, it was shown that the Switcher is not susceptible to prompt irradiation burst while no analog voltages are applied. The modules are safe from possible damage in OFF and STANDBY state.
During the irradiation with applied Switcher voltages, increasing current changes were observed between certain channels. This hints to a potential connection and internal current flow.
Investigations of possible protective measures showed, that damage occurs at a threshold voltage of approximately 4 V. Therefore, the reduction of `ClearHIGH` and `GateHIGH` voltages cannot prevent damage under the tested conditions.
The emergency shutdown, as it was used during the presented measurement, is not sufficient to prevent additional Switcher defects even at faster than simultaneous trigger with the incident beam.
Further investigations are ongoing. From PXD side, a fast shutdown board is developed, that uses an active pulldown of system voltages to decrease the shutdown time. A prototype was already tested during the irradiation campaign in July. Due to different discharge behavior during the active shutdown, it caused similar increase in currents and inefficiencies in the tested modules and will be further revised.
In addition, further improvements are planned on the accelerator side. Studies are ongoing to improve the detection of bad beam conditions and allow a faster beam dump.
Both efforts could already be benefitial and could be tested at additional irradiation campaigns at the Mainz Microtron.

Bibliography

[1] *The Standard Model*,
URL: https://home.cern/science/physics/standard-model (visited on 12/10/2020) (cit. on p. 1).

[2] J. Brodzicka et al., *Physics achievements from the Belle experiment*,
Progress of Theoretical and Experimental Physics **2012** (2012), 04D001, ISSN: 2050-3911,
eprint: https://academic.oup.com/ptep/article-pdf/2012/1/04D001/11595832/pts072.pdf,
URL: https://doi.org/10.1093/ptep/pts072 (cit. on pp. 1, 3).

[3] K. Abe et al., *Observation of LargeCPViolation in the NeutralBMeson System*,
Physical Review Letters **87** (2001), ISSN: 1079-7114,
URL: http://dx.doi.org/10.1103/PhysRevLett.87.091802 (cit. on p. 1).

[4] B. Aubert et al., *Observation of CP violation in the B^0 meson system*,
Phys. Rev. Lett. **87** (2001) 091801, arXiv: hep-ex/0107013 (cit. on p. 1).

[5] *The Nobel Prize in Physics 2008*,
URL: https://www.nobelprize.org/prizes/physics/2008/summary/ (visited on 10/29/2020) (cit. on p. 1).

[6] I. Adachi et al.,
Precise Measurement of the CP Violation Parameter $\sin 2\phi_1$ *in* $B^0 \to (c\bar{c})K^0$ *Decays*,
Phys. Rev. Lett. **108** (17 2012) 171802,
URL: https://link.aps.org/doi/10.1103/PhysRevLett.108.171802 (cit. on p. 1).

[7] L. Canetti, M. Drewes, and M. Shaposhnikov, *Matter and antimatter in the universe*,
New Journal of Physics **14** (2012) 095012, ISSN: 1367-2630,
URL: http://dx.doi.org/10.1088/1367-2630/14/9/095012 (cit. on p. 1).

[8] K. Akai, K. Furukawa, and H. Koiso, *SuperKEKB Collider*,
Nuclear Instruments and Methods in Physics Research Section A: Accelerators, Spectrometers, Detectors and Associated Equipment **907** (2018) 188, ISSN: 0168-9002,
URL: http://dx.doi.org/10.1016/j.nima.2018.08.017 (cit. on pp. 1, 6).

[9] T. Kamitani et al., "SuperKEKB Positron Source Construction Status,"
5th International Particle Accelerator Conference, 2014 MOPRI004 (cit. on p. 3).

[10] T. Abe et al., *Belle II Technical Design Report*, 2010,
arXiv: 1011.0352 [physics.ins-det] (cit. on pp. 3, 6, 10–12, 14–17).

[11] *SuperKEKB and Belle II Project*,
URL: https://www.belle2.org/project/super_kekb_and_belle_ii (visited on 12/10/2020) (cit. on pp. 4, 9).

[12] M. Tanabashi et al., *Review of Particle Physics*, Phys. Rev. D **98** (3 2018) 030001,
URL: https://link.aps.org/doi/10.1103/PhysRevD.98.030001 (cit. on p. 4).

[13] V. Lüth, *A challenge to lepton universality in B meson decays*,
Hyperfine Interactions **239** (2018), ISSN: 1572-9540,
URL: http://dx.doi.org/10.1007/s10751-018-1531-1 (cit. on p. 4).

[14] S. H. Robertson, *The Belle II Experiment*,
Journal of Physics: Conference Series **1271** (2019) 012011,
URL: https://doi.org/10.1088%2F1742-6596%2F1271%2F1%2F012011 (cit. on p. 4).

[15] I. Adachi et al., *sBelle Design Study Report*, 2008, arXiv: 0810.4084 [hep-ex] (cit. on p. 4).

[16] F. Müller, *Characterization and optimization of the prototype DEPFET modules for the Belle II Pixel Vertex Detector*, 2017,
URL: http://nbn-resolving.de/urn:nbn:de:bvb:19-210714
(cit. on pp. 5, 13, 16, 18–23, 25, 26).

[17] T. Abe et al., *Achievements of KEKB*, PTEP **2013** (2013) 03A001 (cit. on pp. 5, 6).

[18] H. Koiso et al., *Lattice of the KEKB colliding rings*,
Progress of Theoretical and Experimental Physics **2013** (2013), 03A009, ISSN: 2050-3911,
eprint: https://academic.oup.com/ptep/article-pdf/2013/3/03A009/4440102/pts086.pdf,
URL: https://doi.org/10.1093/ptep/pts086 (cit. on p. 6).

[19] *SuperKEKB collider achieves the world's highest luminosity*,
URL: https://www.kek.jp/en/newsroom/2020/06/26/1400/ (visited on 10/26/2020) (cit. on p. 6).

[20] T. Uglov, *Neutral long-living kaon and muon system of the Belle II detector*,
Astroparticle, Particle, Space Physics and Detectors for Physics Applications (2014),
URL: http://dx.doi.org/10.1142/9789814603164_0066 (cit. on p. 10).

[21] S. Sandilya, *Particle Identification with the TOP and ARICH detectors at Belle II*, 2017,
arXiv: 1706.08515 [physics.ins-det] (cit. on p. 10).

[22] S. Iwata et al., *Particle identification performance of the prototype aerogel RICH counter for the Belle II experiment*,
Progress of Theoretical and Experimental Physics **2016** (2016) 033H01, ISSN: 2050-3911,
URL: http://dx.doi.org/10.1093/ptep/ptw005 (cit. on p. 11).

[23] U. Tamponi, *The TOP counter of Belle II: status and first results*, 2018,
arXiv: 1811.04532 [hep-ex] (cit. on p. 11).

[24] E. Torassa, *Particle identification with the TOP and ARICH detectors at Belle II*, Nuclear Instruments and Methods in Physics Research Section A: Accelerators, Spectrometers, Detectors and Associated Equipment **824** (2016) 152, Frontier Detectors for Frontier Physics: Proceedings of the 13th Pisa Meeting on Advanced Detectors, ISSN: 0168-9002, URL: http://www.sciencedirect.com/science/article/pii/S0168900215013789 (cit. on p. 11).

[25] *SuperKEKB official web page, CDC design*, URL: https://www2.kek.jp/proffice/archives/feature/2010/BelleIICDCDesign.html (visited on 11/23/2020) (cit. on p. 12).

[26] M. Friedl et al., *The Belle II Silicon Vertex Detector*, Physics Procedia **37** (2012) 867, Proceedings of the 2nd International Conference on Technology and Instrumentation in Particle Physics (TIPP 2011), ISSN: 1875-3892, URL: http://www.sciencedirect.com/science/article/pii/S1875389212017804 (cit. on p. 12).

[27] A. Moll, *Comprehensive study of the background for the Pixel Vertex Detector at Belle II*, 2015, URL: http://nbn-resolving.de/urn:nbn:de:bvb:19-191067 (cit. on p. 15).

[28] R. Richter et al., *Design and technology of DEPFET pixel sensors for linear collider applications*, Nuclear Instruments and Methods in Physics Research Section A: Accelerators, Spectrometers, Detectors and Associated Equipment **511** (2003) 250, Proceedings of the 11th International Workshop on Vertex Detectors, ISSN: 0168-9002, URL: http://www.sciencedirect.com/science/article/pii/S0168900203018023 (cit. on p. 15).

[29] J. Kemmer and G. Lutz, *New detector concepts*, Nuclear Instruments and Methods in Physics Research Section A: Accelerators, Spectrometers, Detectors and Associated Equipment **253** (1987) 365, ISSN: 0168-9002, URL: http://www.sciencedirect.com/science/article/pii/0168900287905183 (cit. on p. 16).

[30] R. Kohrs et al., *A DEPFET Pixel Vertex Detector for TESLA Proposal and Prototyping Report*, (2020) (cit. on p. 16).

[31] S. Rummel, *Investigation of DEPFET as Vertex Detector at ILC – Intrinsic properties, radiation hardness and alternative readout schemes*, Dissertation: Technische Universität München, 2009 (cit. on p. 16).

[32] N. Wermes et al., *New results on DEPFET pixel detectors for radiation imaging and high energy particle detection*, IEEE Transactions on Nuclear Science **51** (2004) 1121, ISSN: 0018-9499, URL: http://dx.doi.org/10.1109/TNS.2004.829490 (cit. on pp. 16, 18).

[33] L. Andricek et al., *Spatial resolution analysis of micron resolution silicon pixel detectors based on beam and laser tests*, Nuclear Instruments and Methods in Physics Research Section A: Accelerators, Spectrometers, Detectors and Associated Equipment **604** (2009) 385, PSD8Proceedings of the 8th International Conference on Position Sensitive Detectors, ISSN: 0168-9002 (cit. on p. 16).

[34] L. Andricek et al., *Advanced testing of the DEPFET minimatrix particle detector*, Journal of Instrumentation **7** (2012) C01101 (cit. on p. 17).

[35] D. Collaboration, *The PXD Whitebook*, (2017) (cit. on p. 17).

[36] J. Knopf, *Development, Characterization and Operation of the DCDB, the Front-End Readout Chip for the Pixel Vertex Detector of the Future BELLE-II Experiment*, URL, PhD thesis, 2011, URL: http://www.ub.uni-heidelberg.de/archiv/12706 (cit. on pp. 18, 21).

[37] P. Fischer, C. Kreidl, and I. Perić, *SwitcherB18 (Gated Mode) Reference Manual*, (2015) (cit. on pp. 19–21).

[38] I. Perić, *Production ASICs: DCDB4.1 and DCDB4.2 Reference Manual*, (2016) (cit. on p. 22).

[39] M. Lemarenko, L. Germic, and T. Hemperek, *Data Handling Processor Manual*, (2016) (cit. on p. 22).

[40] P.Leitl, private communication, 2020 (cit. on p. 28).

[41] H.Ye, private communication, 2020 (cit. on p. 29).

[42] *The Mainz Microtron*, URL: https://www.blogs.uni-mainz.de/fb08-nuclear-physics/accelerators-mami-mesa/the-mainz-microtron/ (visited on 11/30/2020) (cit. on p. 31).

[43] H. Herminghaus et al., *The design of a cascaded 800 MeV normal conducting C.W. race track microtron*, Nuclear Instruments and Methods **138** (1976) 1, ISSN: 0029-554X, URL: http://www.sciencedirect.com/science/article/pii/0029554X76901452 (cit. on p. 31).

[44] *The Mainz Microtron Development and Operation*, URL: https://www.blogs.uni-mainz.de/fb08-nuclear-physics/accelerators-mami-mesa/the-mainz-microtron/b1-development-and-operation/ (visited on 11/30/2020) (cit. on p. 31).

[45] *The Mainz Microtron Operation Principle*, URL: https://www.blogs.uni-mainz.de/fb08-nuclear-physics/accelerators-mami-mesa/the-mainz-microtron/operation-principle/ (visited on 11/30/2020) (cit. on pp. 31, 32).

[46] S. Lee, *Accelerator Physics: Second Edition*, World Scientific, 2004, ISBN: 9789813102033, URL: https://books.google.de/books?id=FO87DQAAQBAJ (cit. on p. 32).

[47] T. Walcher, *The Mainz microtron facility MAMI*, Progress in Particle and Nuclear Physics **24** (1990) 189, ISSN: 0146-6410, URL: http://www.sciencedirect.com/science/article/pii/014664109090016W (cit. on p. 32).

[48] *The Mainz Microtron History*, URL: https://www.blogs.uni-mainz.de/fb08-nuclear-physics/accelerators-mami-mesa/the-mainz-microtron/history/ (visited on 11/30/2020) (cit. on p. 32).

[49] M.Hoek, private communication, 2020 (cit. on p. 33).

[50] *Trigger Logic Unit*,
URL: https://twiki.cern.ch/twiki/bin/view/MimosaTelescope/TLU (visited on 12/03/2020) (cit. on p. 35).

[51] *Gaussian Function*, URL: https://mathworld.wolfram.com/GaussianFunction.html (visited on 12/03/2020) (cit. on p. 38).

[52] *Stopping Power Table for Electrons*,
URL: https://physics.nist.gov/PhysRefData/Star/Text/ESTAR.html (visited on 12/03/2020) (cit. on p. 39).

[53] I.Peric, private communication, 2020 (cit. on p. 49).

APPENDIX A

Additional Information

A.1 MAMI Delay

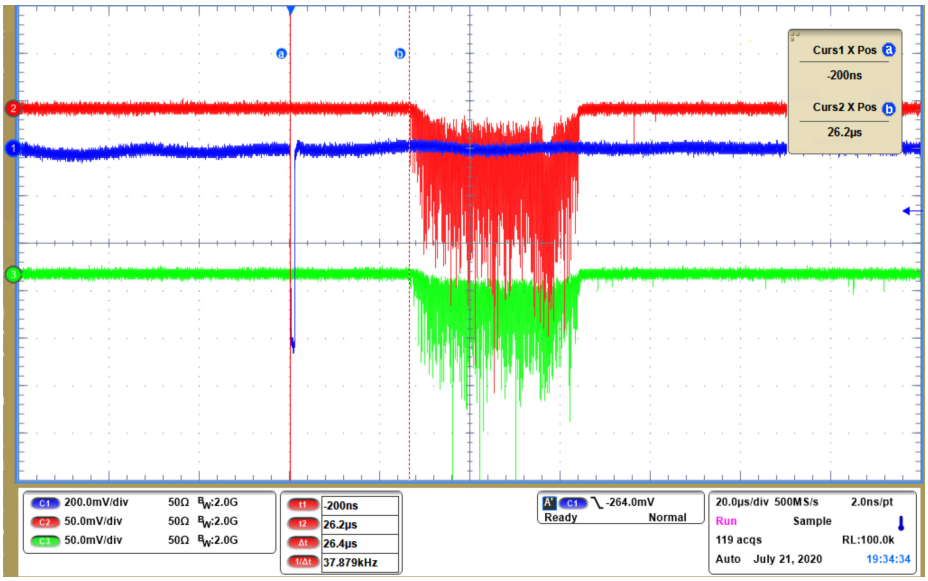

Figure A.1: Oscilloscope screenshot of the MAMI timing. CH1 shows the trigger of the pulse generator for the accelerator. The irradiation burst is measured with two scintillators (CH2/CH3) behind the DUT with a delay of 26.4 µs.

A.2 Voltages and Powering Scheme

AGND	DGND	Gate-GND	Steer-GND
DCD-AVDD	SW-DVDD	**GateOn / `GateLOW`**	**ClearOn / `ClearHIGH`**
DCD-REFIN	DHP-CORE	**GateOff / `GateHIGH`**	**ClearOff / `ClearLOW`**
DCD-AMPLOW	DHP-IO	CCG1, CCG2, CCG3	Bulk
SOURCE	DCD-DVDD	Drift	HV (Backplane)
			Guard
			SW-SUB and SW-REFIN

Table A.1: Distribution of LMU PS voltages over four different domains. Each domain is referenced to a dedicated ground potential. Currents that are monitored with the external Raspberry Pi/Oscilloscope current monitoring are highlighted.

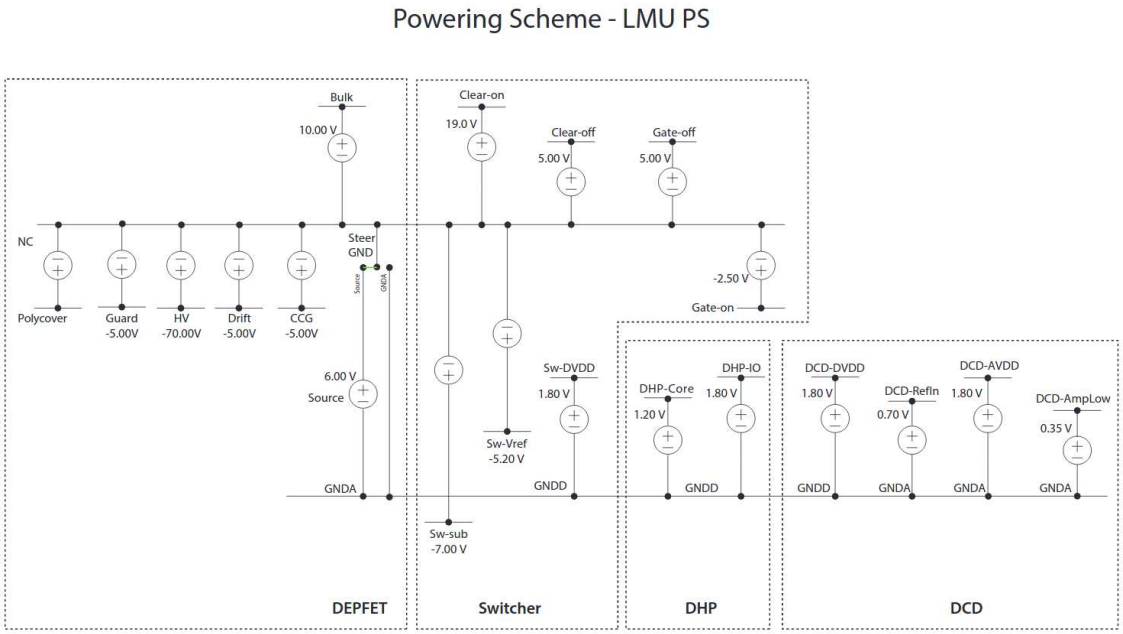

Figure A.2: Sketch of the LMU PS output potentials and their reference voltages including standard voltages for each line.

A.3 Beam Spot Values

H5031	$FWHM_{hor}$ in mm	$\Delta FWHM_{hor}$ in mm	$FWHM_{ver}$ in mm	$\Delta FWHM_{ver}$ in mm
07_27_013	1.000	0.019	0.780	0.004
07_27_020	1.005	0.020	0.732	0.005
07_27_021	0.989	0.020	0.714	0.005
07_27_026	1.026	0.028	0.754	0.015
H5029				
07_22_018	0.986	0.025	0.675	0.008
07_22_019	0.975	0.025	0.660	0.009
07_23_003	0.969	0.024	0.759	0.011
07_23_004	0.970	0.023	0.784	0.011
07_23_005	0.975	0.022	0.797	0.012
07_23_007	0.987	0.024	0.763	0.012
07_23_033	0.972	0.043	0.803	0.031
07_23_035	0.966	0.034	0.768	0.023
07_23_038	0.879	0.014	0.692	0.009
07_23_039	0.872	0.012	0.667	0.008
07_23_040	0.886	0.017	0.677	0.007
07_23_046	1.072	0.031	0.765	0.018

Table A.2: Results of the beam size determination for the two Hybrids H5029 and H5031. These values are used in section 7.1.1 to calculate the average FWHM that is used in the dose rate estimation in 7.1.2.

A.4 Oscilloscope Screenshots of Beam Loss Area Ratio

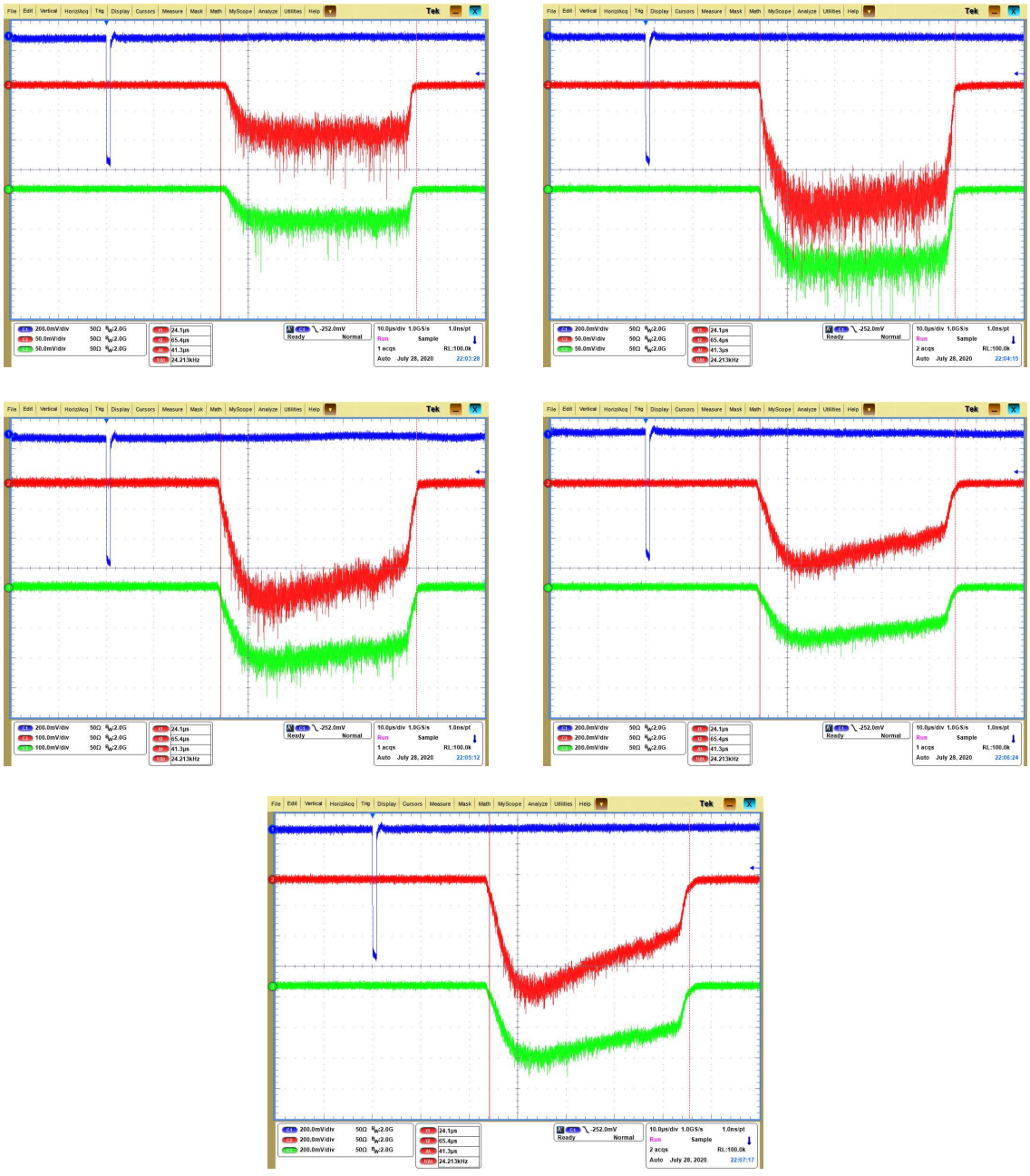

Figure A.3: Oscilloscope picture of the scintillator traces during the irradiation campaign in July 2020. The blue pulse indicates the trigger for the MAMI accelerator. Red and green are the signals of two scintillator located behind the DUT. By comparing the area under the curve to an ideal rectangular shape, a correction factor for beam losses in the machine can be estimated. Beam current from top left to bottom: 1 µA, 2.5 µA, 5 µA, 7 µA, 10 µA.

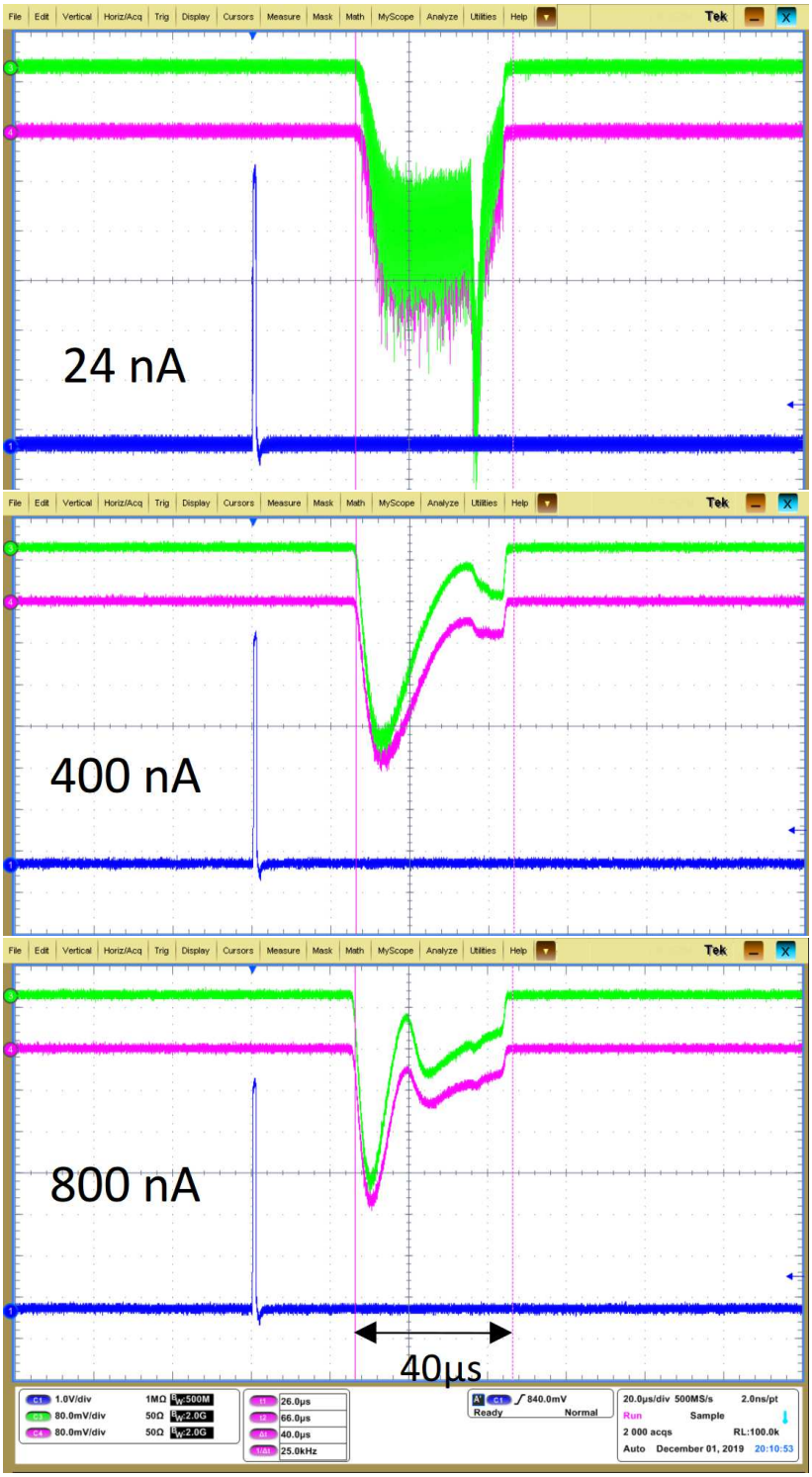

Figure A.4: Oscilloscope picture of the scintillator traces during the irradiation campaign in November 2019. The blue pulse indicates the trigger for the MAMI accelerator. Green and purple are the signals of two scintillator located behind the DUT. By comparing the area under the curve to an ideal rectangular shape, a correction factor for beam losses in the machine can be estimated. Beam current from top to bottom: 24 nA, 400 nA, 800 µA. During this first campaign the accelerator was not optimized for the pulsed operation yet, leading to higher losses in the machine.

List of Figures

List of Tables

Acronyms

ARICH	Aerogel Ring Imaging Cherenkov Detector. 10
CDC	Central Drift Chamber. 11
CM	Common Mode. 22
DEPFET	Depleted P-channel Field-Effect Transistor. 1, 15
DHE	Data Handling Engine. 23, 35
DUT	Device Under Test. 31, 34
ECL	Electromagnetic Calorimeter. 10
FWHM	Full Width Half-Maximum. 38–40, 49
HER	High Energy Ring. 3, 4
IP	Interaction Point. 15, 25
IR	Interaction Region. 15
KEK	High Energy Accelerator Research Organization from japanese kō-enerugī kasokuki kenkyū kikō. 3
KEKB	KEK-B-factory. 3
KLM	K_l and muon counter. 10
LER	Low Energy Ring. 3, 4
LMU PS	LMU (Ludwig-Maximilians-Universität München) Power Supply. 23
MAMI	Mainz Microtron. 2, 31
MOSFET	Metal-Oxide-Semiconductor Field-Effect Tranistor. 16
NIM	Nuclear Instrumentation Module. 34
NIST	National Institute of Standards and Technology. 39
PCB	Printed Circuit Board. 23
PXD	Pixel Vertex Detector. 1, 12, 15
RPi	Raspberry Pi. 36

RTM	Race Track Microtron. 31, 33
SiPM	Silicon Photomultiplier. 10
SLAC	Stanford Linear Accelerator Center. 1
SM	Standard Model of Particle Physics. 1
SVD	Silicon Vertex Detector. 12
TID	Total Ionizing Dose. 37
TOP	Time of Propagation Detector. 11
VXD	Vertex Detector. 12

Acknowledgements

First, I want to thank Prof. Dingfelder for giving me the opportunity to carry out this interesting research project over the course of my master thesis.
Furthermore, I want to thank Prof. Desch for accepting to be the second examiner.

Without Botho's supervision it would have been impossible to perform the measurements presented. Not only for the challenging understanding and operation of the DEPFET system, but also for all other types of problems he always managed to give a good advice.
Apart from Botho, also Georgios helped in intense days and nights during the irradiation campaigns in Mainz. Although it was a lot of work, we managed to have a good time and achieve important results.
From the Mainz accelerator site I would like to thank Dr. Matthias Hoek for organizing and preparing the irradiation campaigns.
Thanks Patrick, for being the perfect office neighbor, giving helpful hints and doing all the service work.
Special thanks also to Pascal for investing a lot of his time, breaking down python basics to me and providing help for the Raspberry Pi readout.
I appreciate the feedback of all those, who offered their help in proofreading. In particular I would like to thank Botho, Georgios, Merlin, Pascal and Patrick.
Even though the Corona situation restricted contacts over large parts of the last year, the SiLab group managed to provide a perfect environment. I really enjoyed working with all of you.
Finally, I want to thank my family for always supporting me. Without your contribution, I would not have been able to achieve any of this.